Multiscale study of microstructural evolution in alkali-activated fly ash-slag paste at elevated temperatures

Wenlin Tu [a], Guohao Fang [b,*], Biqin Dong [c], Mingzhong Zhang [a,*]

[a] Department of Civil, Environmental and Geomatic Engineering, University College London, London WC1E 6BT, UK

[b] Institute for Advanced Study, Shenzhen University, Shenzhen 518060, China

[c] School of Civil Engineering, Guangdong Province Key Laboratory of Durability for Marine Civil Engineering, The Key Laboratory on Durability of Civil Engineering in Shenzhen, Shenzhen University, Shenzhen 518060, China

Abstract: To promote the high-temperature application of alkali-activated fly ash-slag (AAFS), it is vital to thoroughly understand the performance of AAFS at elevated temperatures. This paper presents a systematic study on the multiscale microstructural evolution in AAFS paste in terms of nanostructure, chemical composition and morphology changes characterised using ^{29}Si nuclear magnetic resonance, X-ray diffraction and Fourier transform infrared spectroscopy, as well as the pore structure evolution by means of mercury intrusion porosimetry, backscattered electron microscopy and X-ray microcomputed tomography. Results indicate that the decomposition of C-A-S-H and N-C-A-S-H gels occurs while gel pores are filled at elevated temperatures up to 800 °C, along with the crack development, whereas micro-cracks are healed by melting and viscous sintering. This study provides an in-depth insight into the damage mechanisms of AAFS paste at elevated temperatures from a multiscale viewpoint, accounting for Level I: solid gel particles, Level II: gel matrix, and Level III: AAFS paste.

Keywords: Alkali-activated materials; Geopolymer; Nanostructure; Microstructure; 3D pore structure; Damage evolution

1. Introduction

Alkali-activated materials (AAM) are recognised as promising alternatives to Portland cement (PC), as they not only lead to 60-80% less CO_2 emissions during manufacture which can boost sustainability of construction materials, but also possess superior thermal stability and high-temperature resistance [1-4]. In recent years, a lot of attentions have been placed on the application of AAM as fire protection materials and thermal insulators [5, 6]. The commonly studied AAM can be classified into two categories: (1) single-precursor system such as alkali-activated fly ash (AAF), alkali-activated metakaolin (AAMK) and alkali-activated slag (AAS), and (2) blended precursor system such as alkali-activated fly ash-slag (AAFS) and alkali-activated slag-metakaolin. Among them, AAF

* Corresponding authors.
E-mail addresses: guohao.fang@szu.edu.cn (G. Fang); mingzhong.zhang@ucl.ac.uk (M. Zhang)

exhibits superior mechanical performance after exposure to 800 °C [7-9], attributed to the porous matrix structure with internal-connected channels, which prevents the vapour pressure accumulation at high temperatures [10-12]. AAMK tends to form a more compact and denser internal structure with less pore evolution at elevated temperatures, resulting in a more serious pore pressure-induced damage compared to AAF [8, 13]. Due to the additional hydrated phases formed because of the high calcium content of slag, AAS suffers from a significant strength reduction as the decomposition of $CaCO_3$ can take place at around 756 °C [12, 14, 15]. Thus, AAF is considered as a good choice for high temperature scenarios. However, the in-situ application of AAF is extensively impeded since the activation of fly ash requires heat curing of 60-85 °C to gain acceptable early strength [16, 17]. Hence, a blended system (i.e., AAFS) cured at ambient temperature is introduced, as the incorporation of slag can enhance the degree of alkaline activation of fly ash at ambient temperature [7, 18, 19].

Different from AAF, a more compact internal structure can be found in AAFS at ambient temperature, due to the acceleration of reaction process with the presence of slag [2]. In recent years, the behaviour of AAFS at elevated temperatures has been increasingly studied in terms of mechanical performance and thermal properties. The strength changes of AAFS followed a similar trend to that of AAF. A strength gain of up to around 25% could be detected in AAFS, owing to the further geopolymerisation with consumption of unreacted fly ash particles after 400 °C exposure [12, 20, 21]. Whereas, a significant strength loss (approximately 25-50% of the original strength) in AAFS occurred due to the decomposition of reaction products from 400 to 800 °C [22]. Moreover, viscous sintering could take place at around 800-1000 °C, leading to densification of AAFS matrix and thus the residual strength of AAFS could be slightly recovered [23-25]. In terms of thermal deformation, the increase of slag content in AAFS could lead to a more significant shrinkage in comparison with AAF [26]. For AAFS after exposure to 800 °C, the shrinkage was found to be approximately 4%, which could reach over 25% for paste with 100% slag [27, 28].

Regarding microstructural evolution, only few studies have attempted to explore the phase transformation and physical changes of AAFS at elevated temperatures. AAFS paste is considered as a multiphase heterogeneous composite material, consisting of unreacted fly ash and slag particles, reaction products and pores [16]. Hence, the microstructural features of AAFS can be characterised at three different levels, as schematically illustrated in **Fig. 1**. Level I denotes the nanostructure of solid gel particles that are the elementary components of crystalline and amorphous phases in AAFS [16, 29-31]. The addition of a calcium source leads to the coexistence of N-A-S-H and C-A-S-H gels, with partial replacement of sodium from N-A-S-H gel to form N-C-A-S-H gel that has a higher degree of cross-linking [2, 32-34]. These three types of reaction products dominate the AAFS paste, which take up more than 90% of the binder weight [34]. Level II corresponds to the chemical composition of the AAFS gel matrix, which is agglomerated by the solid gel particles and gel pores. Level III

stands for AAFS paste at micro-scale, composed of gel matrix, unreacted fly ash and slag particles and pores. To systematically understand the microstructural evolution of AAFS at elevated temperatures, it is vital to investigate both individual phase assemblage from nano- to micro-scale and pore structure characteristics.

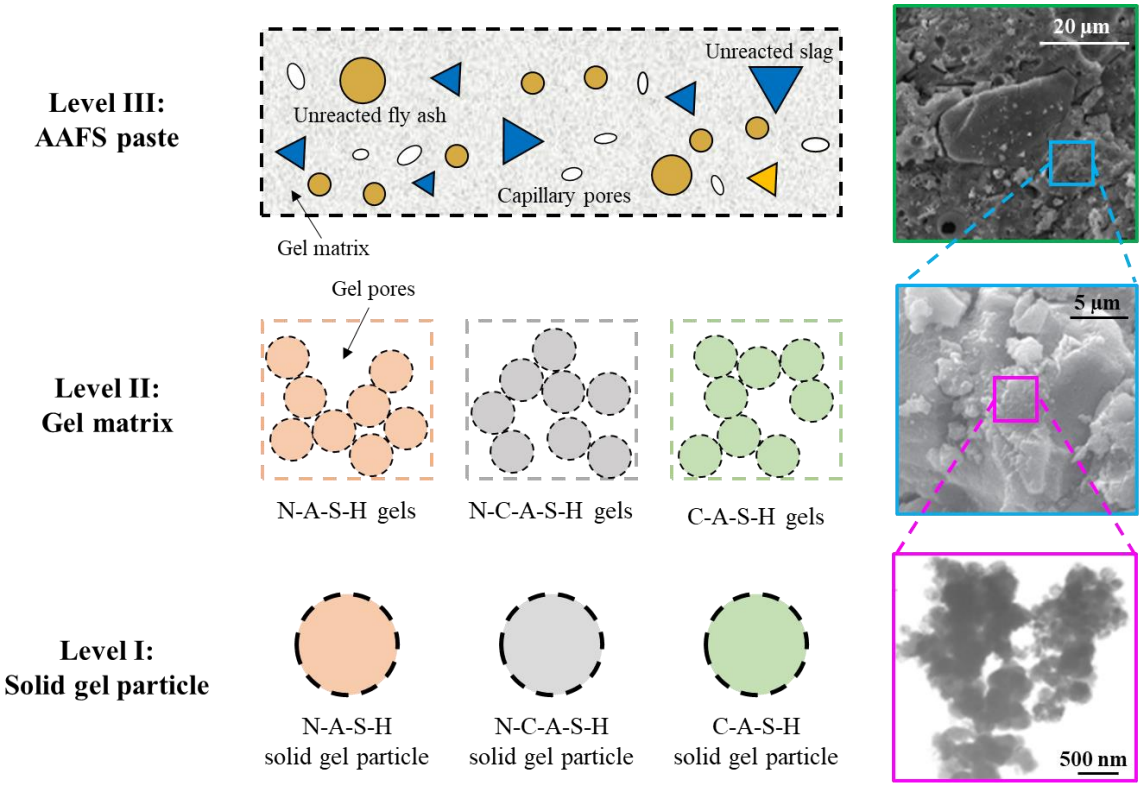

Fig. 1. Schematic diagram of multiscale microstructure of AAFS paste (adapted from Refs. [16, 35-37]).

To date, the nanostructure of AAFS regarding different reaction products at elevated temperatures has been rarely studied and the phase assemblage needs to be thoroughly understood. The previous ^{29}Si nuclear magnetic resonance (NMR) results of AAFS after 400 °C exposure indicated the presence of C-(A)-S-H, which was vulnerable at elevated temperatures, as the dehydration of C-(A)-S-H gel would cause thermal instability along with strength loss [1]. Simultaneously, highly cross-linked N-A-S-H gel with Q^3 and Q^4 structures was formed with the reduction of unreacted glassy phase Si from fly ash. After exposure to 800 °C, the intensity of resonance corresponding to C-A-S-H was found to drop significantly. However, the evolution of solid gel particles in nanostructure of AAFS at elevated temperatures has not been extensively studied yet [7] and the statistical analysis of the changes in reaction products of AAFS at various temperatures is still lacking. As for the chemical compositions of gel matrix in AAFS at Level II, new phases such as akermanite, gehlenite, anorthite and nepheline were reported at 800 °C, depending on the slag content [1, 7, 12, 20, 21]. In terms of pore structure evolution, AAFS experienced the reduction of porosity with diameter of 0.005-6 μm after up to 400 °C exposure, which can be ascribed to the further reaction of residual fly ash particles. At 800 °C, the pore size of AAFS matrix went up (pore diameter > 6 μm), along with the disappearance of C-S-

H gel [7]. Up to now, the existing studies on microstructural characteristics of AAFS were mainly focused on ambient temperature, while the damage evolution in AAFS at elevated temperatures has not been explored from a multiscale and 3D point of view. Therefore, it is vital to fill in the gap of knowledge and provide new insights into the underlying damage mechanisms of AAFS subjected to elevated temperatures.

To this end, this paper aims to systematically investigate the multiscale microstructural evolution of AAFS paste at elevated temperatures. A series of advanced characterisation techniques including NMR, X-ray diffraction (XRD), Fourier transform infrared spectroscopy (FTIR) were undertaken to characterise the nanostructures and phase assemblage of AAFS paste after exposure to various temperatures (20, 105, 200, 400, 600 and 800 °C) at Levels I and II. Meanwhile, the microstructural evolution of AAFS paste in terms of morphology changes, crack development and pore structure characteristics were monitored using backscattered electron microscopy (BSEM), mercury intrusion porosimetry (MIP) and X-ray microcomputed tomography (XCT). Based on the obtained experimental results, the inherent mechanisms of damage evolution in AAFS at elevated temperatures were analysed and discussed in depth from a multiscale point of view.

2. Experimental program

2.1 Raw materials

Low-calcium (Class F) fly ash and ground granulated blast-furnace slag were used as precursors, the chemical compositions of which measured by means of X-ray fluorescence spectrometry (XRF) are presented in **Table 1**. As per a previous study [38], a mixture of 10 M sodium hydroxide (SH) and sodium silicate (SS) was used as alkaline activators, where SH solution was prepared by incorporating 400 g NaOH pellets (analytical level of 99 wt.%) into 1 L water. It was then stored for 24 h to release heat and cool down to ambient temperature before mixing. The modulus (molar ratio of SiO_2/Na_2O) of SS solution (Na_2O: 8.5 wt.%, SiO_2:27.0 wt.%, H_2O: 64.5 wt.%) was set as 2.0. The polycarboxylate-based superplasticiser (SP, Sika®ViscoFlow®2000) was added to ensure the workability of AAFS mixtures [16, 31, 38, 39].

Table 1 Chemical compositions (wt%) of fly ash and slag.

Oxide	SiO_2	Al_2O_3	Fe_2O_3	CaO	K_2O	MgO	TiO_2	Na_2O	SO_3	P_2O_5	MnO
Fly ash	47.51	28.68	7.28	8.02	1.52	1.46	1.00	1.05	0.68	2.35	-
Slag	32.61	16.90	0.33	39.61	0.30	7.28	0.55	0.38	-	0.03	0.26

2.2 Mix proportion

The mix proportion of AAFS paste adopted here was obtained based on the previous studies [29, 40], which can meet the criteria for engineering application in terms of fresh and hardened properties (e.g., workability, setting time and 28 d compressive strength) in accordance with ACI M318-05 [41, 42]. The fly ash-to-slag ratio, alkaline activator-to-precursor (AL/P) ratio, SS-to-SH ratio and SP-to-

precursor (SP/P) ratio were set as 4, 0.4, 0.2 and 0.01, respectively. The Na_2O content was kept as 7.78 wt.% of the precursors (equivalent to 5.5 wt.% of the whole mixture). The mixture quantity is given in **Table 2**.

Table 2 Mix proportion of AAFS.

	Fly ash	Slag	SH	SS	SP
Weight (kg/m^3)	320	80	53	107	4

Note: SH – sodium hydroxide; SS – sodium silicate; SP – superplasticiser.

2.3 Sample preparation

The mixing process of AAFS paste includes two steps: dry mix of fly ash and slag for 3 min, and incorporating SS, SH and SP into the mixture and mixing for another 3 min. The fresh AAFS paste was cast into the cylindrical plastic moulds (⌀15 × 100 mm) after mixing, and placed on a vibrating table for 2 min. The AAFS paste specimens were then sealed with plastic film and cured in a standard curing room (20 ± 2 ºC, 95% relative humidity) for 28 d before testing.

After 28 d, the small cylindrical samples (⌀15 × 5 mm) were cut by operating a low-speed diamond saw with wet-cutting system. The position was kept the same when cutting different samples to ensure the representativeness. After cutting and high temperature exposure, the solvent exchange method was used to stop hydration inside the specimen, which is a commonly used method to eliminate free water from the hardened specimens with negligible impact on its inner microstructure [31]. The isopropanol solution was prepared as the organic solvent. The specimens were then placed in the isopropanol solution for 48 h to ensure free water was removed. Afterwards, the samples were stored in the vacuum drying rack for another 48 h before testing.

To obtain a comparatively smooth surface for BSEM tests, further preparation was required to fill the pores on the testing samples by impregnating epoxy solution. This process was to smoothen the surface and stabilise the microstructure of specimens without alteration when subjected to grinding and polishing [31]. At first, the epoxy solution was prepared by mixing Part A (epoxy resin) with Part B (hardening agent) solution with a mass ratio of Part A/Part B = 3. After stirring for 3-5 min, the vacuum impregnation was performed in a vacuum mosaic containing the testing specimen (i.e., it was placed in a plastic mould with a diameter of 30 mm to ensure the top surface was fully impregnated by epoxy). Finally, the specimen was stored in a vacuum drying rack for 24 h and then demoulded after the epoxy got hardened.

2.4 Heating method

After 28 d of curing, the surfaces of specimens were dried and cleaned prior to heating. Herein, the heating rate was set as 10 °C/min to attain the target temperatures of 105, 200, 400, 600 and 800 °C, apart from ambient temperature. The samples were placed in an electrical furnace with a computed heating curve. When the target temperature was reached, it was maintained for 120 min to ensure

uniform distributed temperatures within the specimen, and thus a thermal equilibrium state can be achieved [43]. Afterwards, the specimen was naturally cooled down to room temperature.

2.5 Testing methods

2.5.1 Nuclear magnetic resonance (NMR)

To characterise the nanostructure of AAFS paste, ^{29}Si NMR test was performed to study the reacted AAFS paste prior to and after high temperature exposure. It can be used to analyse the structural compositions of unreacted particles and reaction products by revealing the silicate structure in binding gels [1, 7, 16, 44]. Herein, the solid-state ^{29}Si NMR instrument (BRUKER, AVANCE 400WB, Germany) was used under the conditions: ^{29}Si resonance frequency of 79.48 MHz, spinning speed of 5 kHz, pulse length of 4.97 μs and a relaxation delay of 5 s with 2048 scans. The powder samples (< 40 μm) were prepared for this test.

2.5.2 X-ray diffraction (XRD)

The phase compositions of AAFS specimens were detected by means of XRD [16, 43]. Similar to NMR test, powder specimens with size of less than 40 μm were used for XRD measurement. To estimate and quantify the amorphous phases of AAFS prior to and after high temperature exposure, the internal standard method of QXRD was also applied. Herein, the XRD instrument (XRD, D8 ADVANCE, Malvern Panalytical, Netherlands) was used under the conditions: CuKα X-ray radiation at the intensity of 40 kV- 40 mA with the slit system of RS = 0.1 mm and DS = SS = 0.6°; the 2θ scanning rate of 6°/min. The step size was set as 0.02° with $2\theta = 90°$.

2.5.3 Fourier transform infrared spectroscopy (FTIR)

Powders smaller than 25 μm were prepared, using a Shimadzu, IR Tracer-100 (Japan). 16 times of scanning from 4000 to 400 cm^{-1} with a resolution of 4 cm^{-1} were performed.

2.5.4 Backscattered electron microscopy (BSEM)

The morphology changes and phase assemblage of AAFS paste were characterised using BSEM. AAFS paste specimens experienced grinding and polishing after the vacuum impregnation using a machine (BUEHLER, EcoMetTM 250, USA). Grinding was performed for 5 min at 50 r/min with a loading of 5 N with ethyl alcohol as a cooling medium and lubricant using paper grits of 400 (37 μm), 800 (19 μm) and 1200 (15.3 μm). Polishing was performed for 15 min at 70 r/min using diamond suspensions with grits of 2500 (5.5 μm), 3000 (5 μm), 5000 (2.7 μm) and 7000 (1.25 μm). Ultrasonic cleaning was applied after these operations and the polished specimens were stored in vacuum bags until testing. A schematic illustration of sample preparation process is given in **Appendix A**.

Before the BSEM test, a thin layer of carbon coating was applied on the specimen to improve the conductivity. During the test, the working distance was 10 mm with the acceleration voltage set as 15 kV and the spot size of 6 nm. BSEM images (pixel size of 20 nm) were obtained at a magnification ranging from 30× to 4000×.

2.5.5 X-ray microcomputed tomography (XCT)

To acquire the 3D microstructural evolution of AAFS paste at elevated temperatures, XCT test was conducted using XRadia-Micro XCT-400 scope (Zeiss, Germany) at 80 kV and 101 µA (magnification of 0.4×). The scanning time for each test was around 4 h to complete 1001 projections (angle step of 0.144º from -180º to 180º) with an 8 s exposure of every projection. The field of view was 1.5 mm (x = y = z) and the spatial resolution was 13.90 µm (x = y = z).

2.5.6 Mercury intrusion porosimetry (MIP)

The pore structure of AAFS paste was characterised using MIP (AutoPore IV 9500). The pore diameters ranging from 0.001 µm to 1000 µm were measured with MIP. The pressure applied for MIP test was from 0 to 414 MPa. The surface tension of mercury employed here was 0.485 N/m. The contact angle between the mercury and the pore surface was 130° [45].

3. Results

3.1 Nanostructure of AAFS solid gel particles at elevated temperatures

The ^{29}Si NMR spectra was obtained to investigate the nanostructure of AAFS solid gel particle at ambient and high temperatures. To determine the chemical surroundings of silicon tetrahedra in different phases, Q^n(mAl) structure units were commonly employed (*n* is the number of oxygen bridges between different silicon tetrahedral and *m* represents the number of aluminium tetrahedra) [46]. The ^{29}Si NMR spectra of fly ash and slag were deconvolved and depicted in **Fig. 2a** and **b**. The presence of fly ash particles was reflected by five Q^4 structures in an overlapped peak: Q^4(4Al) (-87 ppm), Q^4(3Al) (-95 ppm), Q^4(2Al) (-103 ppm), Q^4(1Al) (-110 ppm) and Q^4(0Al) (-116 ppm). On the other hand, a broad peak at approximately -75 ppm was shown in slag particles, which can be assigned to the presence of Q^0 and Q^1 sites [16]. Two traces of signals corresponding to Q^2(1Al) and Q^3(1Al) sites were also found at -83 and -88 ppm, respectively [47].

To monitor and characterise the evolution of reaction products in AAFS at different temperatures, the Q sites from the raw materials were assumed to be stable, while the relative changes of intensities were corresponding to the development of different reaction products, including C-A-S-H, N-C-A-S-H and N-A-S-H gels. **Fig. 2c** displays the ^{29}Si NMR spectrum of AAFS paste at ambient temperature, with deconvolution of the signals that can be assigned to the presence of several Q sites based on the previous NMR studies of AAFS [7, 33, 44, 48]. The spectrum exhibited a broad peak between -70 and -100 ppm, implying a significant portion of Q^0 (unreacted slag), Q^1 and Q^2 (C-A-S-H) from the slag solely and Q^3 (highly cross-linked N-C-A-S-H) from the reaction of both raw precursors. The coverage area between -90 and -120 illustrates the presence of Q^4 (N-A-S-H and unreacted fly ash) sites. The location of different Q^n sites can be referred to the previous NMR analysis [16], which is summarised in **Table 3**. There was a notable drop of Q^2 and Q^3, whereas the

amount of Q^4(3Al) in AAFS went up remarkably as the temperature rises from 20 to 800 °C. The quantification of different phases based on the deconvolution results is also presented in **Table 3**.

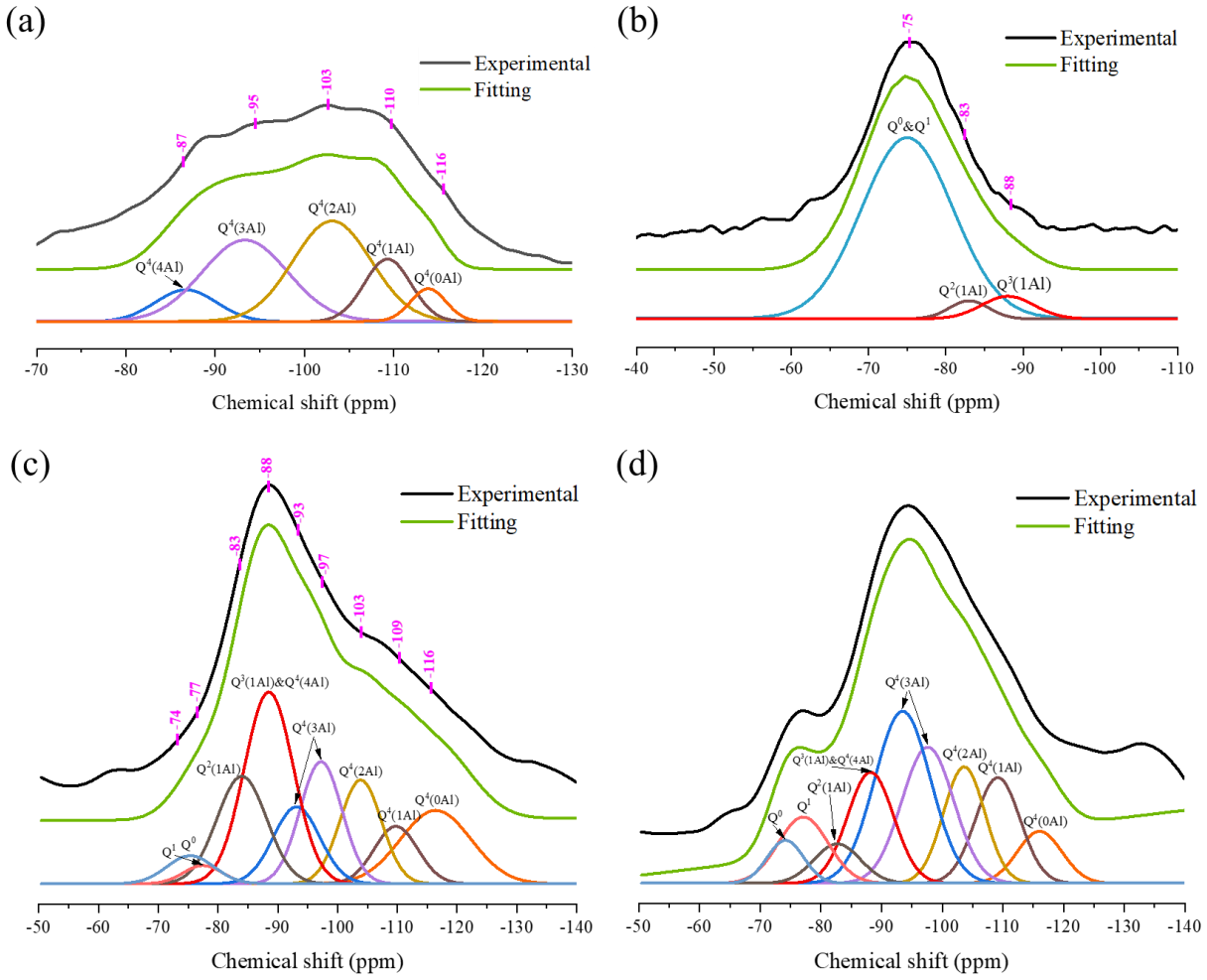

Fig. 2. ^{29}Si NMR spectra of (a) fly ash, (b) slag, and AAFS paste at (c) ambient temperature and (d) 800 °C.

Table 3 Area percentages of ^{29}Si NMR spectra of AAFS paste at elevated temperatures.

Temperature (°C)	Unreacted slag	Reaction products							Unreacted fly ash
		C-A-S-H		N-C-A-S-H	N-A-S-H (Al-rich)		N-A-S-H (Si-rich)		
	Q^0	Q^1	Q^2(1Al)	Q^3(1Al) & Q^4(4Al)	Q^4(3Al)		Q^4(2Al)	Q^4(1Al)	Q^4(0Al)
	-74	-77	-83	-88	-93	-97	-103	-109	-116
20	3.53	1.90	14.24	25.14	9.56	13.68	11.48	6.67	13.81
105	5.17	7.98	20.80	20.35	15.56	10.43	7.87	6.84	5.00
200	5.68	7.07	24.52	21.77	7.10	14.35	5.36	9.48	4.66
400	8.27	16.45	17.01	16.65	10.10	11.48	9.13	5.81	5.12
600	5.97	10.31	11.61	15.09	8.58	26.91	5.04	11.31	5.18
800	3.85	8.21	4.50	12.69	23.81	17.52	11.95	11.71	5.75

With respect to the evolution of different phases in AAFS paste at different temperatures, the ^{29}Si NMR spectra is shown in **Fig. 3**. As the temperature rose from ambient to 200 °C, the broad peak at Zone b was slightly shifted to a lower value from -88.39 to -86.39 ppm, followed by a right shift of

the peak at -94.38 ppm after 800 °C exposure. This indicated the increase in the intensity of sites corresponding to C-A-S-H gel from 20 to 200 °C and a considerable drop with the dehydration of C-A-S-H gel when the temperature exceeded 400 °C [49]. By further evaluating of the AAFS nanostructure changes at elevated temperatures, the volume fractions of Q^n(mAl) structure units corresponding to unreacted particles and reaction products are presented in **Fig. 4**. An increase of the content of Q^2(1Al) from 14.24% to 24.52% can be found after 200 °C exposure. From 400 to 800 °C, the amount of Q^2(1Al) sites went down to 4.5%, suggesting that C-A-S-H gels were no longer the dominant reaction products in AAFS at 800 °C. This is in good agreement with the previous studies, which reported the mitigation of the peaks assigned to C-S-H gel in the XRD pattern of AAFS at 400 °C [7, 50]. The decomposition of C-A-S-H gels and the formation of N-A-S-H gels occurred simultaneously [7, 51, 52], with a reduction of Q^4(0Al) sites from 13.81% to 5.75% and an increase of Q^4(3Al) from 23.24% to 41.33%. Since Q^4(0Al) was assigned to the highly polymerised Al-rich N-A-S-H gel, a higher degree of cross-linking was found in AAFS. This is demonstrated in Zone c of **Fig. 3**, with a right shift of the peak from -107.87 to -110.37 ppm upon exposure at 200 °C and disappearance of the peak after 200 °C exposure. Meanwhile, Q^4(2Al) and Q^4(1Al) sites were recognised to represent more stable Si-rich N-A-S-H types of gel. It is noteworthy that a new peak in Zone a appears at -75.90 ppm after exposed to 800 °C, indicating the formation of gehlenite with monomeric Si [1, 53].

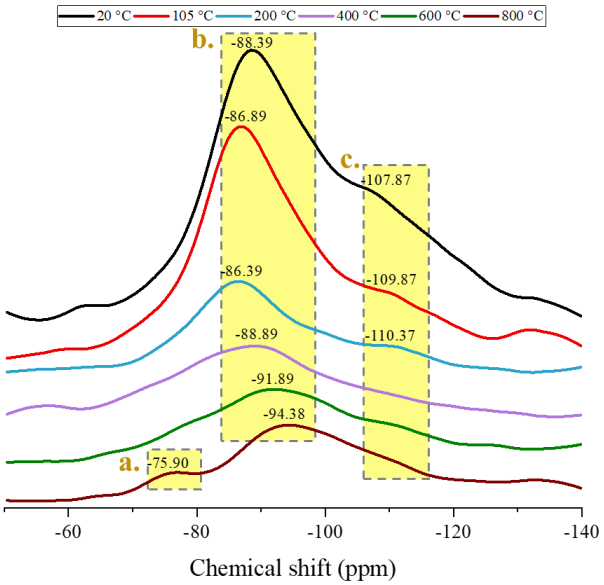

Fig. 3. ^{29}Si NMR spectra of AAFS paste at elevated temperatures.

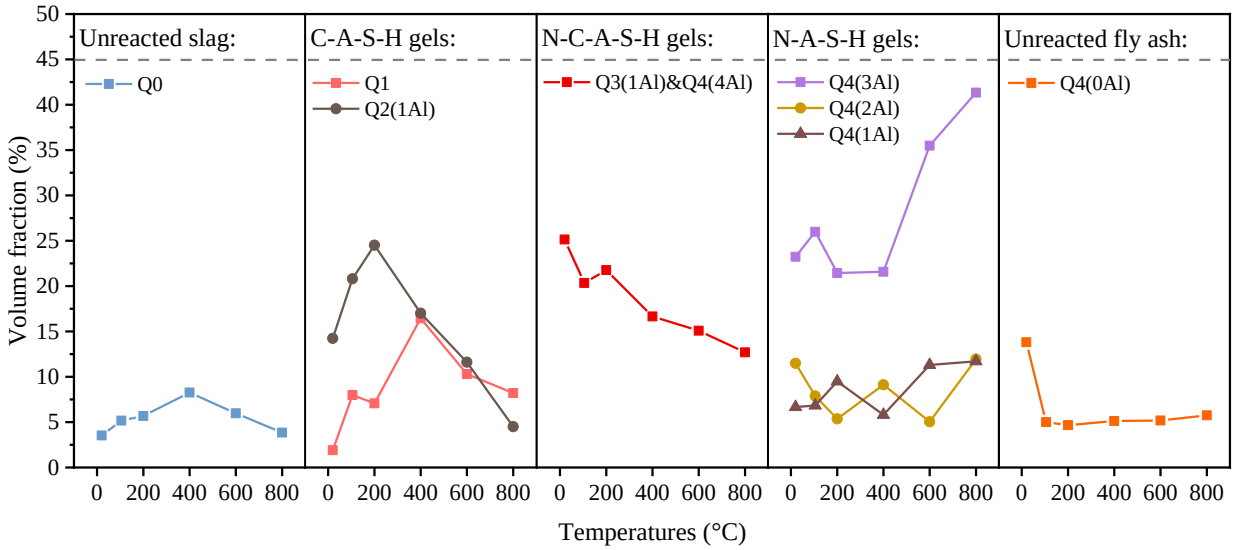

Fig. 4. Volume fractions of different phases in AAFS paste at elevated temperatures.

3.2 Chemical composition of AAFS gel matrix at elevated temperatures

3.2.1 Crystalline phase characterisation

To understand the chemical composition of AAFS gel matrix and track the transformation of different crystalline phases, XRD analysis was carried out to provide the information on AAFS paste at ambient and high temperatures. **Fig. 5a** displays the XRD patterns of raw fly ash and slag. The peaks in the XRD spectra of fly ash were mainly associated with quartz (SiO_2), mullite ($Al_6Si_2O_{13}$) and magnetite (Fe_3O_4), whereas a diffuse band at 25-35° 2θ was depicted in the XRD spectra of slag, corresponding to the presence of glassy phase [1, 54]. **Fig. 5b** shows the XRD results of AAFS paste at different temperatures. At ambient temperature, the crystalline phases presented in AAFS paste were similar to those in the raw fly ash, including quartz, mullite, hematite (Fe_2O_3) and magnetite, which were consistent with those reported in the previous XRD results of AAFS paste [2]. Both quartz and mullite were physically stable when subjected to elevated temperatures, as they had a relatively high melting point of 1713 °C and 1830 °C, respectively [55, 56]. A wide and diffusive band at around 20-35° 2θ reflected the amorphous phases, suggesting the presence of aluminosilicate gels [48]. The peak at around 30° 2θ indicated the presence of calcite [57]. The diffuse hump at around 29-31° 2θ was associated with C-S-H gels, which were formed from the polymerisation of the dissolved active calcium out of slag with silica provided by sodium silicate in a strong alkaline environment [58, 59]. Also, the Si from C-S-H gels could be possibly replaced by Al to form C-(A)-S-H gels [54]. After high temperature exposure, the decrease of the intensity of C-S-H phase was observed at 200 °C, implying the decomposition of C-S-H gels, while no obvious changes can be identified until 800 °C was reached. New crystalline phases including nepheline ($NaAlSiO_4$), gehlenite ($Ca_2Al(AlSiO_7)$) and akermanite ($Ca_2MgSi_2O_7$) can be observed, implying the fully crystallisation and decomposition of N-A-S-H, C-(A)-S-H and hybrid gels at 800 °C. The formation of nepheline was corresponding to the partial crystallisation of N-A-S-H gel, while gehlenite and akermanite were associated with the

transformation of C-(A)-S-H gel. The findings from ^{29}Si NMR also supported that the reduction of C-A-S-H content corresponding to Q^1 and Q^2(1Al) could happen from 200 to 800 °C. Consequently, more cross-linked Q^4 sites occurred, which can be ascribed to the presence of nepheline [1].

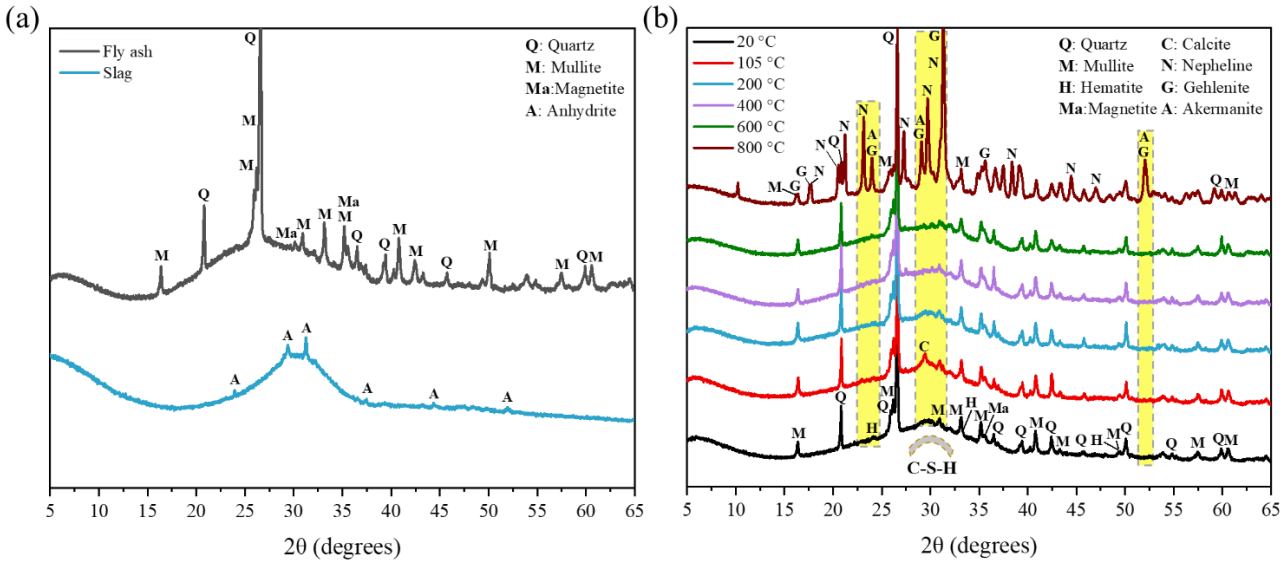

Fig. 5. XRD patterns of (a) precursors, and (b) AAFS paste at elevated temperatures.

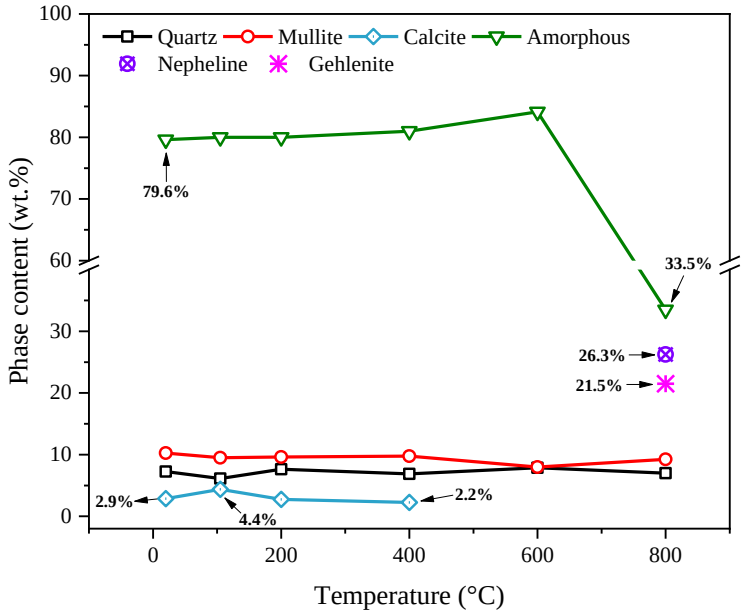

Fig. 6. Mineralogical compositions of AAFS paste at elevated temperatures.

Fig. 6 presents the mineralogical compositions of AAFS paste at elevated temperatures acquired with Rietveld refinement. It can be seen that the crystalline phases of quartz and mullite were thermally stable after 800 °C exposure, which slightly fluctuated around 6.9% and 9.5%, respectively, while the amorphous content dropped dramatically from 79.6% to 33.5% at 800 °C, along with the appearance of nepheline and gehlenite, taking up 26.3% and 21.5%, respectively. This indicated that the partial recrystallisation of amorphous aluminosilicates in AAFS paste was approximately 57.9% of the total amorphous phase. As nepheline was formed from the crystallisation of N-A-S-H gel, while the formation of gehlenite was associated with the crystallisation of C-A-S-H gel, the calculated phase

content implied that the crystalline phase transformation of AAFS paste at 800 °C could be more sensitive to N-A-S-H induced phases [60]. Furthermore, it is worth noting that the content of calcite went up from 2.9% to 4.4% when the temperature rose to 105 °C, followed by a drop to 2.2% at 400 °C. After 400 °C, calcite was not detected in AAFS paste, indicating the decomposition of this phase, as mentioned above.

3.2.2 Amorphous phase identification

FTIR test results can be used to study the chemical changes of AAFS paste at elevated temperatures. **Fig. 7** illustrates the FTIR spectra of raw precursors and AAFS paste at different temperatures. As seen in **Fig. 7a**, the major band at around 1008 cm^{-1} can be observed in raw fly ash, which was associated with the asymmetric stretching vibration of Si-O-T bonds, where T stood for Si or Al units [60, 61]. The band ranging from around 680 to 800 cm^{-1} corresponded to the stretching vibrations of Si-O-Si and the weak peak at 1486 cm^{-1} could be ascribed to the O-C-O bonds associated with the presence of calcite [2, 60]. Similar to raw fly ash, the main band observed at 860 cm^{-1} in slag was related to Si-O-T bonds. The discrepancy between the band positions of fly ash and slag (i.e., 1008 and 860 cm^{-1}) was due to the chemical and structural differences of these two materials [16, 32]. The vibration band at 1488 cm^{-1} can be assigned to the stretching vibration of O-C-O bonds [2], which implied the existence of calcite as confirmed in the XRD patterns in **Fig. 5b**. Moreover, the absorption band observed at around 670 cm^{-1} can be attributed to the T-O stretching vibrations (see **Fig. 7a**).

Fig. 7b demonstrates a comparison among FTIR spectra of AAFS paste at different temperatures. At ambient temperature, the alkali-activation provided an intense band centred at 962 cm^{-1}, assigning to the asymmetric stretching vibrations of Si-O-T bonds. Knowing that C-A-S-H gels were located at 950 cm^{-1} and the wavenumber representing N-A-S-H gels was centred at 1020 cm^{-1}, the position that corresponded to the reaction products of AAFS pastes (i.e. 962 cm^{-1}) was located between C-A-S-H and N-A-S-H gels, implying the coexistence of both types of gels and the presence of N-C-A-S-H gel [16, 32, 36, 62]. With the rise of temperature, the Si-O-T bonds shifted to left towards a higher value of wavenumber, which reached 970 and 993 cm^{-1} at 400 and 800 °C, respectively. This indicated that the formation of C-A-S-H gels could potentially make a pronounced impact on the reaction products in AAFS at 20 °C, since the wavenumber of 962 cm^{-1} was closer to 950 cm^{-1} than 1020 cm^{-1}. However, the rising temperature to up to 800 °C could lead to the promotion of further polymerisation and thus the development of N-A-S-H gels with a higher cross-linking structure (i.e., 993 cm^{-1} was closer to 1020 cm^{-1}) [16]. This was also confirmed in the ^{29}Si NMR results that there was an around 21.3% loss of C-A-S-H gels, while the volume fraction of N-A-S-H gels went up by about 57.1% from 20 to 800 °C. This suggested the transformation of gel matrix in AAFS paste from a potentially C-A-S-H dominated to N-A-S-H dominated structure with the coexistence of N-C-A-S-H, attributing to the presence of Ca from slag. Moreover, the absorption area tended to be broader and deeper as the

temperature went up, indicating a more disordered structure in the AAFS gel matrix due to high temperature exposure, which agreed well with the previous study on AAFS at elevated temperatures [2, 63].

The signal at around 2360 cm^{-1} was assigned to CO_2 vibration, while the vibration band located at around 1670 cm^{-1} was associated with H-O-H bonds that represented both physically- and chemically-bonded water in the gel matrix and disappeared after 400 °C exposure [2, 64, 65]. This indicated that moisture was fully lost in AAFS paste. Similarly, the vibration band at about 1440 cm^{-1} was linked to the carbonates from soluble alkali species, which also became invisible after 600 °C. Furthermore, the highlighted broad band from around 600 to 860 cm^{-1} was recognised as the quartz band, which did not experience an obvious change after high temperature exposure, suggesting the thermal stable feature of quartz, as mentioned in the XRD results [2, 60].

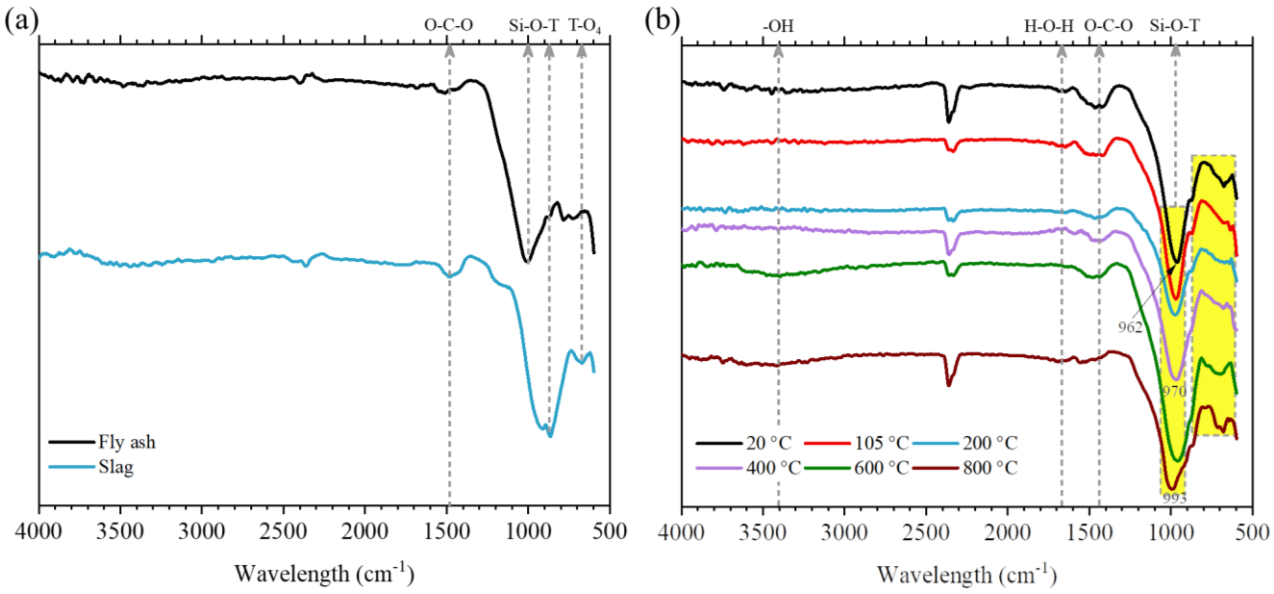

Fig. 7. FTIR spectra of (a) precursors, and (b) AAFS paste at elevated temperatures.

3.3 Microstructure of AAFS paste at elevated temperatures

3.3.1 Solid phase assemblage

The BSEM images of AAFS after high temperature exposure are shown in **Fig. 8**. At 20 °C, both unreacted fly ash and slag particles can be observed. The activation of small fly ash particles was more noticeable than the relatively larger particles, which can be explained by the fact that finer particles were easier consumed and activated than coarser ones at ambient temperature [66, 67]. The dissolution of slag particles at this stage was ascribed to a higher vitreous phase of more than 90% involved in the alkaline activation compared to that of fly ash (around 50% vitreous phase) [16, 66]. Hence, the degree of activation in slag was more pronounced than fly ash, which was consistent with the NMR and FTIR results, confirming the dominant presence of slag induced C-A-S-H gels. Also, there were some visible micro-cracks in AAFS paste at 20 °C, due to autogenous, chemical and drying shrinkage during the curing process [40].

When the exposure temperature went up to 105 °C, the reaction of fly ash and slag particles continued with the initiation and propagation of wider cracks along the edge of unreacted precursors, which implied that the cracks were prone to develop around the interfacial transition zone between unreacted particles and reaction products. The development of cracks at this stage could be resulted from the evaporation of free moisture that led to the propagation and localisation of cracks at the relatively weaker interface [2]. At 200 °C, the unreacted particles were gradually consumed to form hybrid N-C-A-S-H gels. The cracks kept growing due to the loss of physically- and chemically-bound water and the transport of moisture that resulted in the accumulation of pore pressure [26, 68, 69]. Fully activated fly ash and slag particles can be observed in AAFS paste after 400 °C exposure. Some fly ash particles exhibited hollow structures, which may leave a porous spherical-shaped region, as highlighted in **Fig. 8**.

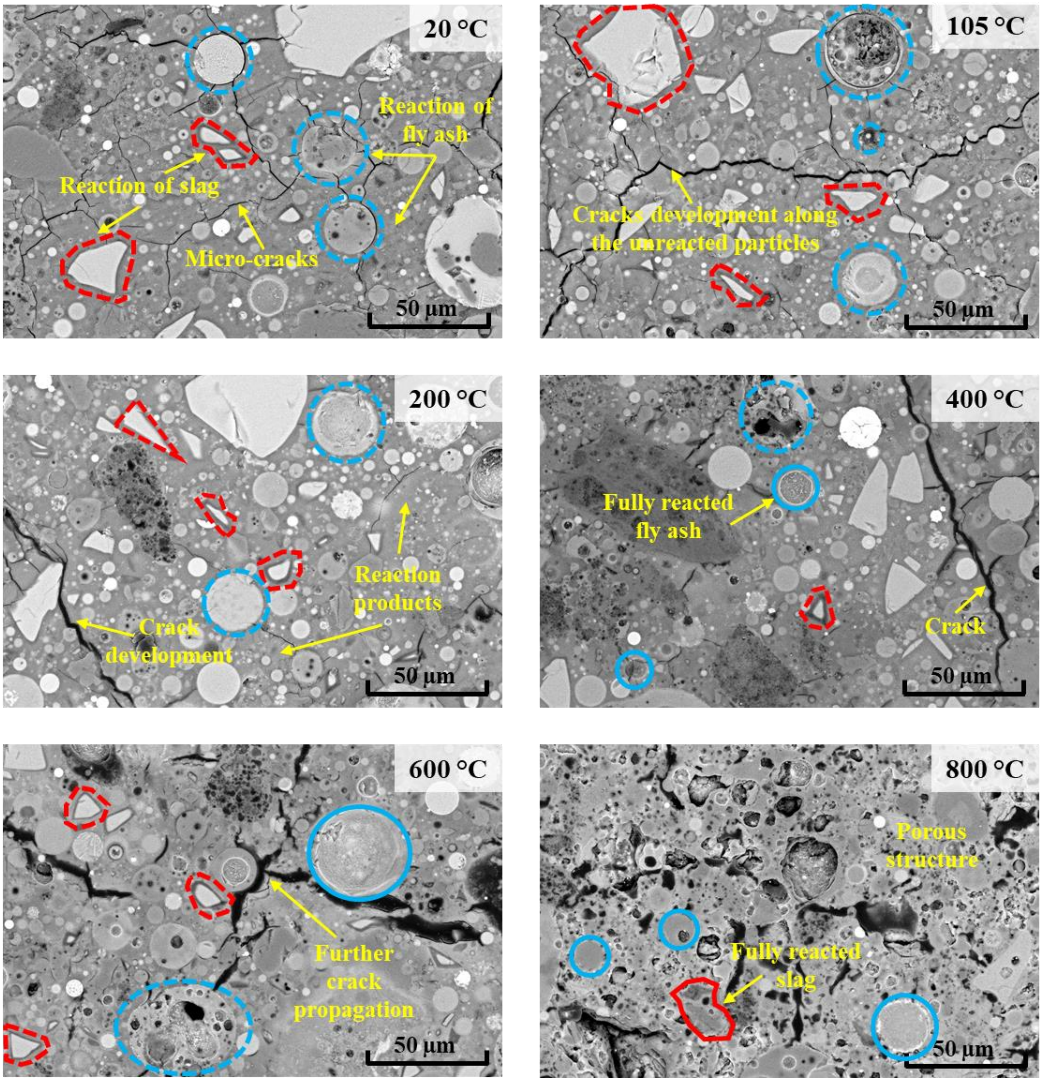

Fig. 8. BSEM images of AAFS paste at elevated temperatures.

After 600 °C exposure, the presence of small and widen cracks indicated that AAFS paste experienced discontinuity due to pore pressure-induced and thermal stress-induced damage, along with decomposition of hybrid gels [2, 69]. In particular, the decomposition of silica gel could take

place at 700-800 °C, resulting in thermal expansion and thus the widening and lengthening of cracks [62, 70, 71]. Slag particles could barely be observed, while some holes were detected on the surface of residual fly ash particles. At 800 °C, a porous structure with traces of consumed precursor particles was shown. There were few unreacted particles at this stage and micro-cracks were not observed. This can be attributed to melting and viscous sintering, which corresponded to the collapse of nano-pores and evolution of interparticle bonding, allowing the self-healing of micro-cracks and densification of AAF matrix by filling small voids [26, 72].

3.3.2 Pore structure

3.3.2.1 Pore size distribution by MIP

Apart from solid phases, a combination of pores, inherent voids and cracks that formed the whole pore structure of AAFS paste was also a crucial phase at the paste level. The evolution of pore structure characteristics of AAFS paste at elevated temperatures obtained from MIP test is presented in **Fig. 9**, where the pore size is defined and categorised into three distinct size ranges for better description: small pores (2-50 nm), medium pores (50-7500 nm) and large pores (> 7500 nm) [2, 73].

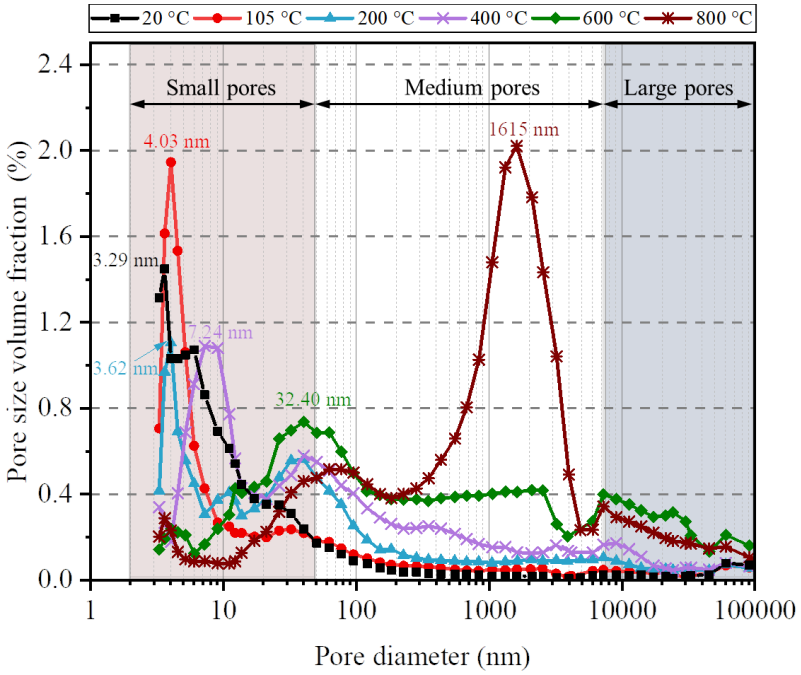

Fig. 9. Pore size distribution of AAFS paste at elevated temperatures.

At ambient temperature, the highest peak appeared with the pore size of 3.29 nm, indicating that originally the majority of the pores formed were gel pores (i.e., ≤ 10 nm). Similarly, the pore sizes corresponding to the highest volume fractions for AAFS exposed to 105 °C and 200 °C were 4.03 nm and 3.62 nm, respectively. After 400 °C, pores with diameter of 7.24 nm dominated the matrix structure. The pore size continued to shift to a larger size of 32.4 nm when subjected to 600 °C, belonging to capillary pores (i.e., 10-50 nm). At this stage, the majority of the pores were distributed between small and medium sizes. When the temperature reaches 800 °C, a broad peak at 1615 nm was detected, implying a sharp and drastic change of pore size distribution from small to medium

pores. **Fig. 10** demonstrates the cumulative pore volume of AAFS at elevated temperatures. In general, the total pore volume fraction (also known as porosity) roughly remained at the original level until 400 °C, followed by a significant increase by more than 10% after 800 °C exposure.

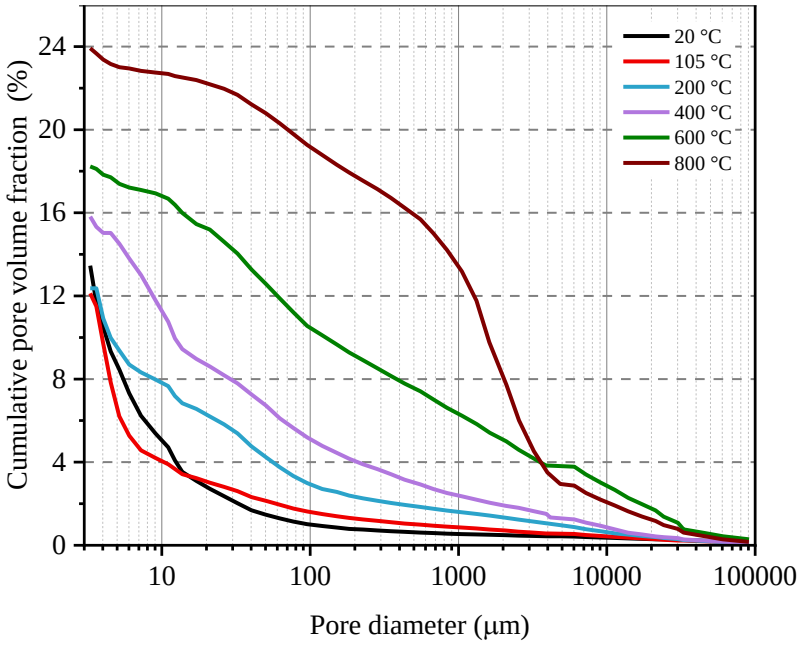

Fig. 10. Cumulative pore volume of AAFS paste at elevated temperatures.

To further estimate the development of pores within different size ranges, **Fig. 11a** provides the compositions of different pores that contribute to the total porosity in AAFS paste at ambient and high temperatures. There was a slight reduction of overall porosity from 13.45% to 12.37 % when the temperature rose from 20 to 200 °C, due to a combined effect of water evaporation and further geopolymerisation that promoted the development of binder gels with a higher cross-linking level and thus resulted in continuous refinement of pores [7, 54]. A relatively significant drop of 16.59% can be observed in the volume fraction of small pores from 105 to 200 °C, implying that the reaction process might be slowed down at this stage as the degree of reactivity was positively proportional to the volume fraction of gel pores [2]. Meanwhile, there was a rise of the proportions of medium and large pores by 20.65% and 2.7%, respectively. This can be attributed to the transport of moisture from heated surface to inner area, allowing the pore pressure build-up that led to the initiation and propagation of microcracks and the development of an inter-connected network in AAFS paste.

From 200 to 600 °C, a great number of medium pores were generated, while a further mitigation of small pores by 38.51% can be found. As seen in the BSEM images, AAFS matrix experienced lengthening and widening of cracks as the exposure temperature went up, confirming the growth of medium and large pores. Simultaneously, the remarkable mitigation of small pores at 600 °C implied that the sintering effect might take place since gel pores could collapse to form larger pores and also, they could be filled by melting and densification [26]. **Fig. 11b** illustrates the detailed proportion of gel and capillary pores within the group of small pores, which confirms a rapid decrease of gel

porosity with rising temperature from 400 to 600 °C. Furthermore, it is noteworthy that the volume of gel pores increased at up to 105 °C, confirming the further reaction process and formation of new binder gels. At 800 °C, the volume fractions of both gel and capillary pores dropped to less than 10%, whereas medium pores became the dominant group with a proportion of 77.72%.

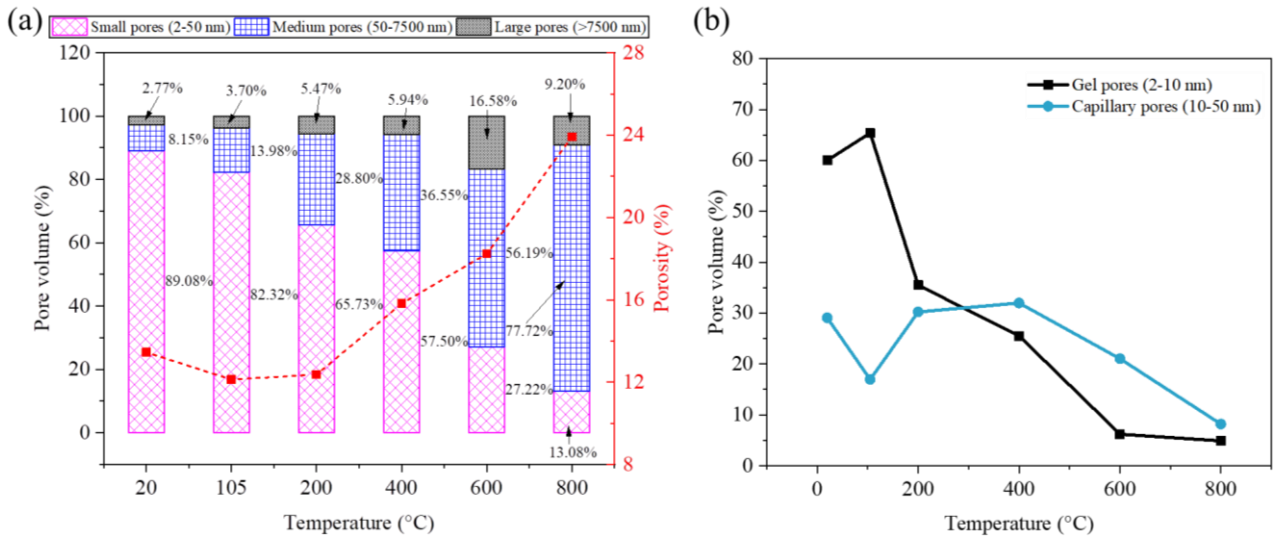

Fig. 11. (a) Pore volume fractions of AAFS paste at elevated temperatures, and (b) detailed pore volume distribution within 2-50 nm.

3.3.2.2 Pore structure characteristics by XCT images

MIP can provide the information on internal pore structure and the formation of cracks by measuring pore throat size, whereas the relatively larger pores with small pore throat size might not be accurately characterised [2, 74-76]. By analysing XCT images, the evolution of larger pores and cracks in AAFS paste could be captured. According to the voxel size of 13.9 µm, the smallest pore that can be detected had an average diameter of 27.8 µm (i.e., a cube is formed by the arrangement of 8 voxels) [77, 78]. After denoising, segmentation, labelling and sieving on the XCT images, the pore structure evolution of AAFS paste at elevated temperatures was obtained and demonstrated in **Fig. 12**. Due to the difficulty of singling out the cracks from the pores since they shared the similar grey value, the label and sieve analysis was performed based on the inter-connected pore volume including both pores and cracks [77].

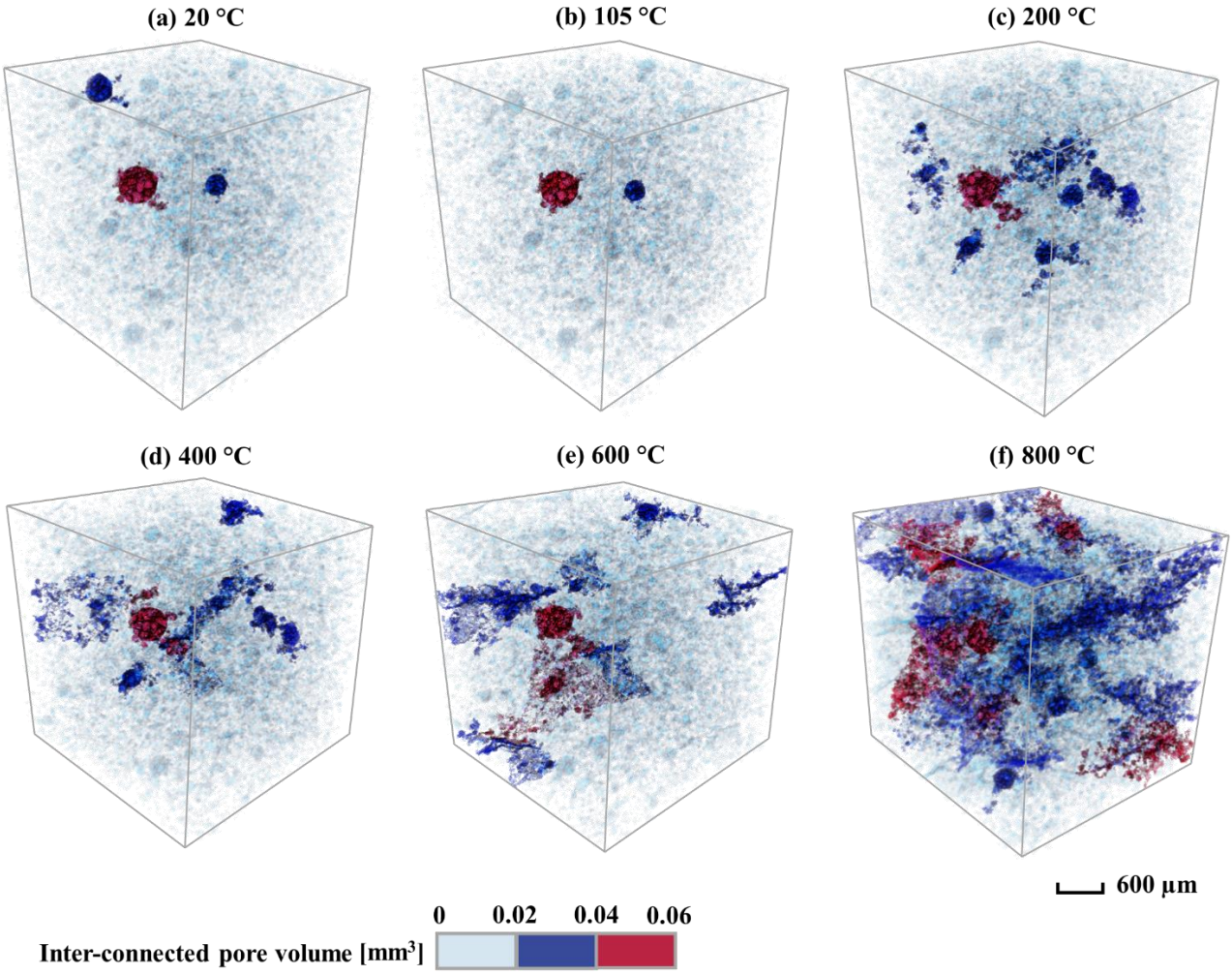

Fig. 12. Evolution of inter-connected pores and cracks in AAFS paste at elevated temperatures obtained from XCT imaging.

The pore volume was categorised into three ranges: 0-0.02 mm^3, 0.02-0.04 mm^3 and 0.04-0.06 mm^3 based on the quantification of pore size distribution, which varied from 0 to 0.06 mm^3 in the shown representative volume element. **Fig. 13** illustrates the size distribution of pores with respect to mean diameter. At up to 105 °C, there were few visible pores with a volume larger than 0.02 mm^3. As the temperature increased to up to 600 °C, the gradual development of inter-connected pore network could be observed. After 800 °C exposure, the number of pores corresponding to 0.02-0.04 mm^3 rose dramatically, while several major cracks and voids could be found, which indicated the drastic deterioration of inner structure in AAFS paste and the increase of internal pore connectivity at 800 °C. The number of pores with diameter of less than 0.1 mm dropped comparatively when the temperature went up from 20 to 800 °C, while the number of pores with diameter of 0.2 mm increased by approximately 300%. Moreover, pores larger than 0.45 mm only existed after 400 °C exposure, which can be associated with the completed water evaporation process and thermal stress induced by temperature gradient.

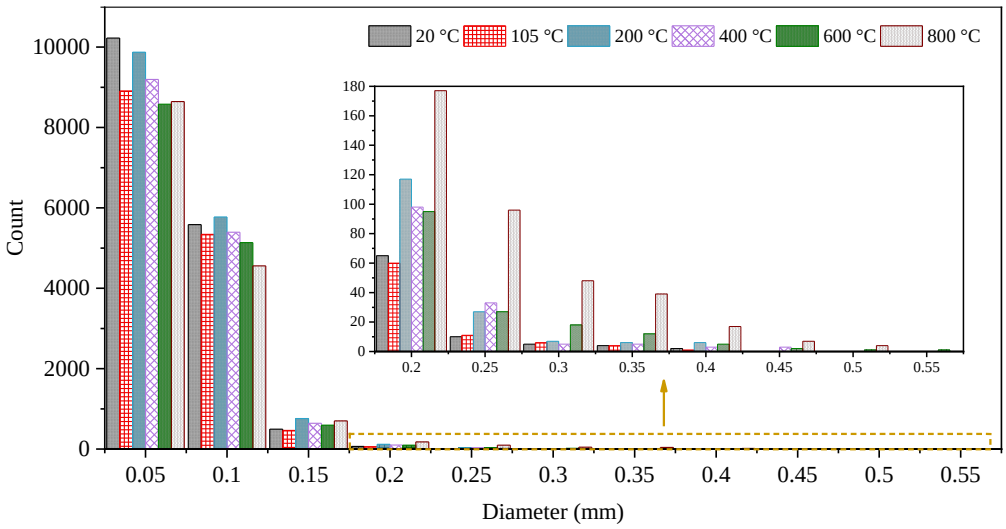

Fig. 13. Pore size distribution of AAFS paste at elevated temperatures obtained from XCT imaging.

4. Discussion

This section further analyses the multiscale microstructural evolution of AAFS paste at elevated temperatures in terms of individual phase assemblage and pore structure characteristics, together with the proposed damage mechanisms corresponding to different levels: Level I - solid gel particles, Level II - gel matrix and Level III - AAFS paste. According to the variations of microstructural features of AAFS paste at elevated temperatures, the discussion can be made as per four different stages: (1) Stage 1: ambient temperature, Stage 2: 20-200 °C, Stage 3: 200-600 °C and Stage 4: 600-800 °C, as schematically illustrated in **Fig. 14**.

At Level I, the importance is attached to the nanostructure of solid gel particles including N-A-S-H, N-C-A-S-H and C-A-S-H particles. At 20 °C, Q^0 and Q^4(0Al) sites are associated with the unreacted precursors, which take up around 17.34% of the total volume. With the reaction of unreacted precursors, the aluminates and silicates are released as monomers after experiencing chemical attack and dissolution [79]. Level II refers to the gel matrix consisting of hybrid gels and gel pores (see **Fig. 14**). At ambient temperature, the gel pores occupy around 60% of the total pore volume based on the MIP results, which indicates that the raw precursors have been significantly consumed to form reaction products, leaving a large number of gel pores in AAFS gel matrix [2]. This is consistent with the assemblage of different phases at Level I. At level III, the focus is placed on paste, composed of unreacted fly ash and slag particles, reaction products and pores (i.e., capillary and larger pores with cracks and voids). A considerable amount of unreacted fly ash particles can be observed in the BSEM images, while some micro-cracks appear at this stage as well, due to shrinkage of AAFS matrix during the curing process. The capillary pores take up approximately 29% of the total porosity, whereas medium and larger pores play less crucial roles at this stage.

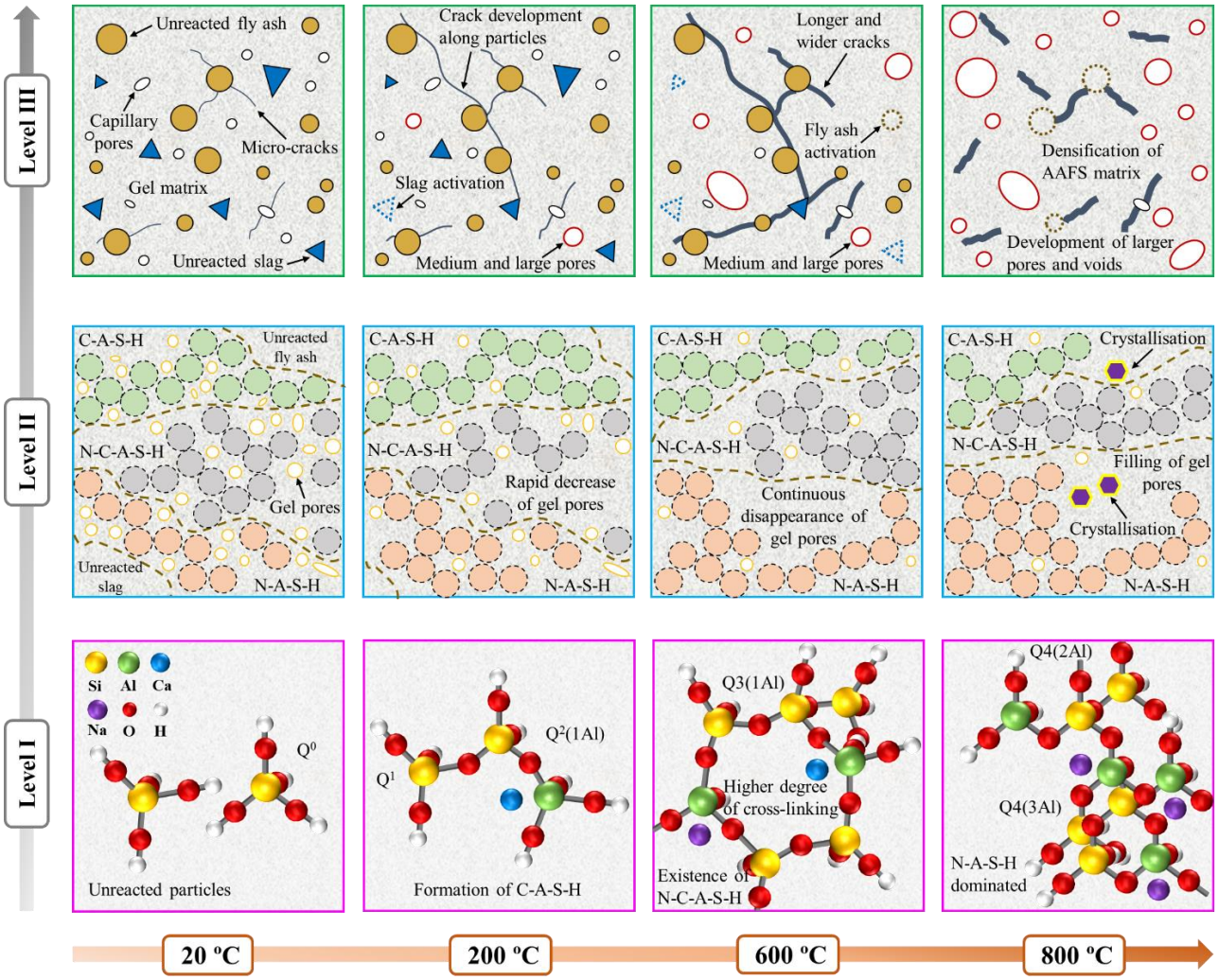

Fig. 14. Schematic diagram of multiscale microstructural evolution of AAFS paste at elevated temperatures.

After 200 °C exposure, there is an obvious increase of Q^2(1Al) sites from 14.24% to 24.52%, ascribed to the formation of C-A-S-H, where Si and Al tetrahedra are bonded together with the presence of Ca^{2+} ions. This indicates the further promotion of slag activation from 20 to 200 °C. As per the ^{29}Si NMR test results, the temperature rise can generally cause the transformation of solid gel particles from lower degree of cross-linking to higher levels. Regarding gel matrix at Level II, there exhibits a rapid drop of gel pore volume fraction from about 65% to 35% due to the further reaction and the refinement of gel pores [54]. Meanwhile, new medium and large pores are generated at Level III, which can be attributed to the water evaporation and moisture transport. Crack development can be observed at this temperature due to the pore pressure-build up. The accumulation of vapour pressure in the pore structure can result in the initiation and propagation cracks, which develop along the weak transition zone between unreacted particles and reaction products [69]. Moreover, AAFS paste can experience thermal-induced tensile stress, leading to the development of new cracks and converging into larger ones [68].

From 200 to 600 °C, an obvious mitigation of Q^2(1Al) by approximately 12.91% can be found. The signals associated with Q^3(1Al) sites at this stage indicate the existence of N-C-A-S-H, so that the main reaction products are composed of N-C-A-S-H and N-A-S-H structures where Si and Al tetrahedra can be bonded with a ring shape with Ca^{2+} and Na^+ ions [79]. As for gel matrix, the disappearance of calcite and C-S-H phase can be observed from the XRD and QXRD results, which is corresponding to the rapid decrease of Q^2(1Al) sites at Level I. There is a continuous loss of gel pores at this temperature, implying further gel pore refinement with disordered gel structures. At Level III, the cracks become widened and lengthened compared to the previous stage. Medium pores dominate the inter-connected network, occupying about 56.2% of the total porosity. This can be ascribed to the viscous sintering with collapse of gel and capillary pores to form larger ones, resulting in densification in the gel matrix at Level II with larger pores observed in the paste at Level III. Especially, pores with diameter of greater than 0.45 mm start to appear after 400 °C exposure, as observed in the XCT images.

After 800 °C, N-A-S-H with Q^4(3Al) dominates the reaction products, with the existence of Q^4(2Al) and Q^4(1Al) sites. Compared with Q^2(1Al) sites, Q^4(3Al) structure shows a higher degree of cross-linking, indicating the concentration of solid gel particles and the decomposition of C-A-S-H gels in AAFS after 800 °C exposure. This was also confirmed in the previous study on binder gels in AAFS at elevated temperatures that the increase of Q^4(nAl) sites revealed the dehydration of C-A-S-H gels at 800 °C, favouring the formation of more cross-linked N-A-S-H gel and new crystalline phases such as anorthite and nepheline (also indicated in the XRD results in this study) [1]. At Level II, gel pores can barely be seen, with less than 5% of the total pore volume (i.e., an around 92.5% reduction from 20 to 800 °C) due to sintering effect. Crystallisation of nepheline and gehlenite happens at this stage, which respectively take up 26.3% and 21.5% of the whole crystalline phases. The formation of nepheline is associated with the highly cross-linked aluminosilicate, while monomeric Si can contribute to the presence of gehlenite [7]. Meanwhile, the amorphous phase drops significantly from more than 80% to 33.5% according to the QXRD results, which also explains the decomposition of hybrid gel while crystallisation happens. On the other hand, FTIR results show a tendency of the main band (assigned to the Si-O-T bonds) shifting from a position of lower to higher wavelength, which also suggests that N-A-S-H becomes the dominant reaction product in AAFS after 800 °C exposure. Both sintering and densification can enhance the compactness of gel matrix, whereas AAFS paste exhibits a more porous structure with flaws and voids due to the drastic matrix deterioration at Level III [2]. The disappearance of micro-cracks can be attributed to the melting and self-healing in AAFS at 800 °C. Overall, the main features about damage evolution in AAFS paste at elevated temperatures are summarised in **Fig. 15**.

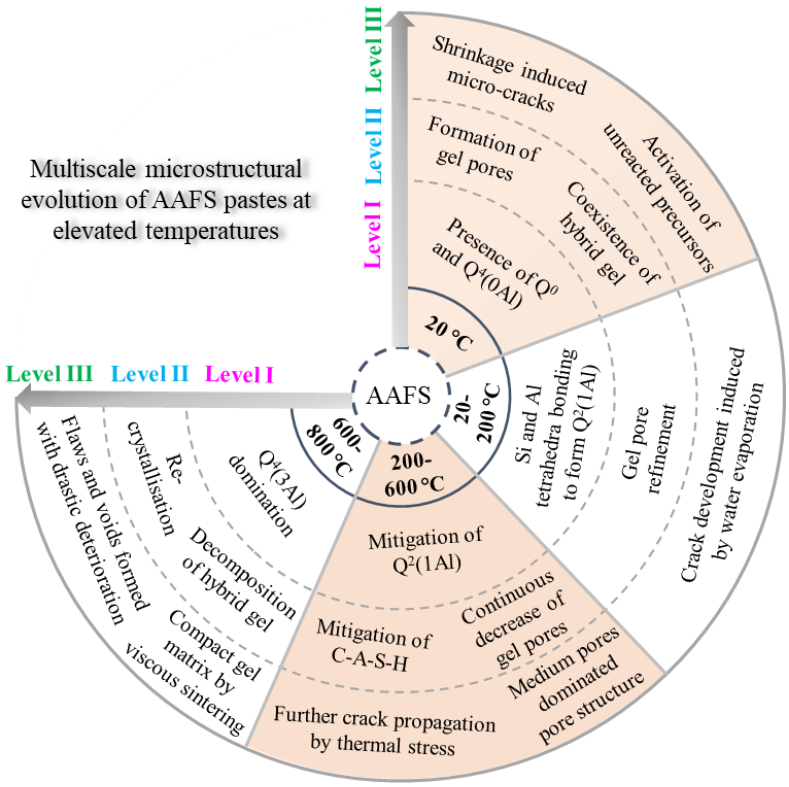

Fig. 15. Multiscale microstructural evolution of AAFS paste at elevated temperatures.

5. Conclusions

In this study, the microstructural evolution in AAFS paste exposed to various temperatures (i.e., 20, 105, 200, 400, 600, and 800 °C) at multiple length scales covering solid gel particles, gel matrix and paste was systematically investigated using a series of advanced characterisation techniques including ^{29}Si NMR, XRD, FTIR, BSEM and MIP. Based on the obtained experimental results, the main conclusions can be drawn as follows:

- The nanostructure of solid gel particles in AAFS was highly sensitive to exposure temperature. At 20-200 °C, the bonding between Si and Al tetrahedra was promoted to form Q^2(1Al) with an over 10% rise in volume fraction. After 600 °C exposure, the proportion of Q^2(1Al) dropped rapidly, along with a jump from around 20% to 34% for Q^4(3Al), indicating the decomposition of C-A-S-H gel to form more cross-linked N-A-S-H gel. At 800 °C, N-A-S-H gel (≥ 40% in volume) dominated the nanostructure of AAFS, while the volume fractions of C-A-S-H and N-C-A-S-H gels reduced considerably to approximately 10% and 12%, respectively.
- The gel matrix in AAFS was composed of hybrid gels and gel pores (2-10 nm), which experienced refinement with a volume mitigation from about 60% to 35% after exposure to 200 °C. With the rise of exposure temperature from 200 to 600 °C, a continuous drop in gel porosity to around 5% took place, which can be attributed to the further reaction that could potentially fill the gel pores. After exposed to 800 °C, new crystalline phases including nepheline and gehlenite can be observed, which took up around 26.3% and 21.5% of the crystalline phases by volume, while the

volume fraction of amorphous phase dropped by more than 46.1%, compared to that at ambient temperature. The Si-O-T bonds corresponding to main reaction products in FTIR spectra tended to shift from C-A-S-H gel to N-A-S-H gel, along with the increase of wavelength from 962 to 993 cm^{-1}, further confirming the decomposition of C-A-S-H gel to form more cross-linked structures.

- At the paste level, the crack development along with the formation of capillary (10-50 nm), medium (50-7500 nm) and large pores (> 7500 nm) occurred due to water evaporation and pore pressure accumulation in AAFS with the rising exposure temperature from 20 to 200 °C. At 600 °C, the pore pressure build-up and thermal stress led to further crack growth and medium pores dominated the pore structure. After exposed to 800 °C, viscous sintering took place, resulting in a more compact gel matrix with gel porosity of less than 5%, along with the decomposition of hybrid gels, while micro-cracks disappeared, attributing to the melting and potential self-healing effect of AAFS at 800 °C.

Acknowledgements

Guohao Fang gratefully acknowledges the financial support from the National Natural Science Foundation of China (Grant No. 52108232) and Shenzhen Key Laboratory for Low-carbon Construction Material and Technology (Grant No. ZDSYS20220606100406016). The financial support provided by University College London (UCL) through a Graduate Research Scholarship to the first author is also greatly appreciated. The authors would also like to thank Mr Guanqi Wei, Mr Ruixi Li, Mr Guohong Wang, Miss Rou Gang, Mr Changzhi Jiang and Miss Huiyin Zhong for their help with the experimental work.

Appendix A. AAFS sample preparation for BSEM tests

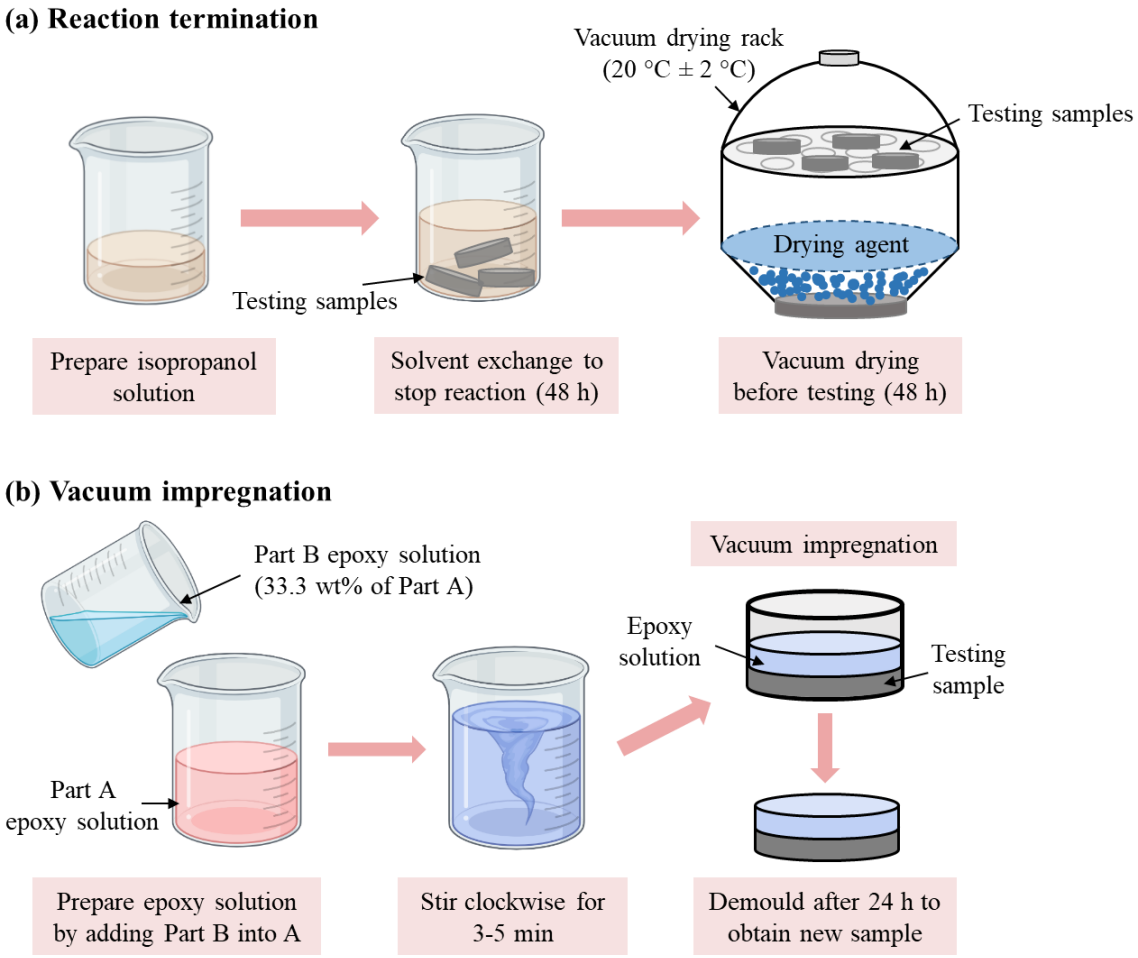

Fig. A1. Schematic illustration of sample preparation process regarding: (a) reaction termination and (b) vacuum impregnation.

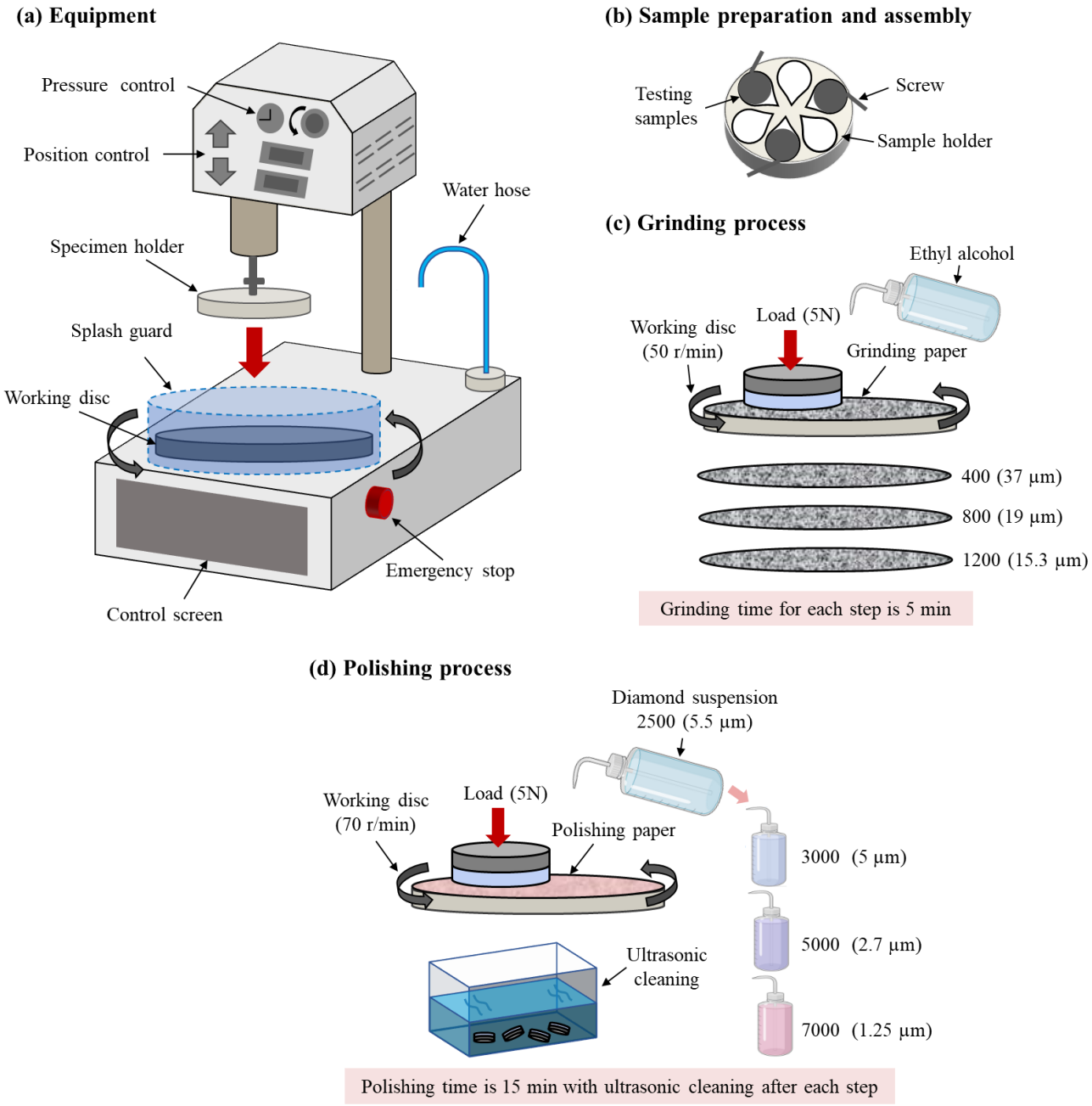

Fig. A2. Schematic illustration of grinding and polishing process.

References

[1] N.K. Lee, K.T. Koh, G.H. An, G.S. Ryu, Influence of binder composition on the gel structure in alkali activated fly ash/slag pastes exposed to elevated temperatures, Ceram Int, 43 (2017) 2471-2480.

[2] Y. Luo, S.H. Li, K.M. Klima, H.J.H. Brouwers, Q.L. Yu, Degradation mechanism of hybrid fly ash/slag based geopolymers exposed to elevated temperatures, Cement Concrete Res, 151 (2022) 106649.

[3] A.M. Rashad, Y. Bai, P.A.M. Basheer, N.C. Collier, N.B. Milestone, Chemical and mechanical stability of sodium sulfate activated slag after exposure to elevated temperature, Cement Concrete Res, 42 (2012) 333-343.

[4] F. Ameri, P. Shoaei, S.A. Zareei, B. Behforouz, Geopolymers vs. alkali-activated materials (AAMs): A comparative study on durability, microstructure, and resistance to elevated temperatures of lightweight mortars, Constr Build Mater, 222 (2019) 49-63.
[5] T.W. Cheng, J.P. Chiu, Fire-resistant geopolymer produced by granulated blast furnace slag, Miner Eng, 16 (2003) 205-210.
[6] A. Buchwald, M. Hohmann, C. Kaps, H. Bettzieche, J.T. Kuhnert, Stabilised foam clay material with high performance thermal insulation properties, Cfi-Ceram Forum Int, 81 (2004) E39-E42.
[7] S.M. Park, J.G. Jang, N.K. Lee, H.K. Lee, Physicochemical properties of binder gel in alkali-activated fly ash/slag exposed to high temperatures, Cement Concrete Res, 89 (2016) 72-79.
[8] H.Y. Zhang, V. Kodur, B. Wu, L. Cao, S.L. Qi, Comparative Thermal and Mechanical Performance of Geopolymers derived from Metakaolin and Fly Ash, J Mater Civil Eng, 28 (2016) 1-13.
[9] J.B. Sundararaj, P.R.K. Rajkumar, M. Sivasakthi, M. Jegan, Effect of mineral admixtures on mechanical and thermal properties of geopolymer mortar at elevated temperature, Innov Infrastruct So, 7 (2022) 354.
[10] Z. Pan, J.G. Sanjayan, B.V. Rangan, An investigation of the mechanisms for strength gain or loss of geopolymer mortar after exposure to elevated temperature, J Mater Sci, 44 (2009) 1873-1880.
[11] Z. Pan, J.G. Sanjayan, F. Collins, Effect of transient creep on compressive strength of geopolymer concrete for elevated temperature exposure, Cement Concrete Res, 56 (2014) 182-189.
[12] Z. Pan, Z. Tao, Y.F. Cao, R. Wuhrer, T. Murphy, Compressive strength and microstructure of alkali-activated fly ash/slag binders at high temperature, Cement Concrete Comp, 86 (2018) 9-18.
[13] P. Duan, C.J. Yan, W. Zhou, W.J. Luo, C.H. Shen, An investigation of the microstructure and durability of a fluidized bed fly ash-metakaolin geopolymer after heat and acid exposure, Mater Design, 74 (2015) 125-137.
[14] O.G. Rivera, W.R. Long, C.A. Weiss, R.D. Moser, B.A. Williams, K. Torres-Cancel, E.R. Gore, P.G. Allison, Effect of elevated temperature on alkali-activated geopolymeric binders compared to portland cement-based binders, Cement Concrete Res, 90 (2016) 43-51.
[15] I.H. Aziz, M.M.A. Abdullah, C.Y. Heah, Y.M. Liew, Behaviour changes of ground granulated blast furnace slag geopolymers at high temperature, Adv Cem Res, 32 (2020) 465-475.
[16] G.H. Fang, M.Z. Zhang, Multiscale micromechanical analysis of alkali-activated fly ash-slag paste, Cement Concrete Res, 135 (2020) 105860.
[17] J.I.E. Garcia, K. Campos-Venegas, A. Gorokhovsky, A. Fernandez, Cementitious composites of pulverised fuel ash and blast furnace slag activated by sodium silicate: effect of Na2O concentration and modulus, Adv Appl Ceram, 105 (2006) 201-208.

[18] X. Gao, Q.L. Yu, H.J.H. Brouwers, Reaction kinetics, gel character and strength of ambient temperature cured alkali activated slag-fly ash blends, Constr Build Mater, 80 (2015) 105-115.
[19] A. Rafeet, R. Vinai, M. Soutsos, W. Sha, Effects of slag substitution on physical and mechanical properties of fly ash-based alkali activated binders (AABs), Cement Concrete Res, 122 (2019) 118-135.
[20] F.L. Qu, W.G. Li, Z. Tao, A. Castel, K.J. Wang, High temperature resistance of fly ash/GGBFS-based geopolymer mortar with load-induced damage, Mater Struct, 53 (2020) 1-21.
[21] S. Celikten, M. Saridemir, I.O. Deneme, Mechanical and microstructural properties of alkali-activated slag and slag plus fly ash mortars exposed to high temperature, Constr Build Mater, 217 (2019) 50-61.
[22] S.J. Chithambaram, S. Kumar, M.M. Prasad, Thermo-mechanical characteristics of geopolymer mortar, Constr Build Mater, 213 (2019) 100-108.
[23] J.R. Ren, H.G. Chen, R.X. Dai, T. Sun, Behavior of combined fly ash/GBFS-based geopolymer concrete after exposed to elevated temperature, 2019 3rd International Workshop on Renewable Energy and Development (Iwred 2019), 267 (2019) 032056.
[24] J.R. Ren, H.G. Chen, T. Sun, H. Song, M.S. Wang, Flexural Behaviour of Combined FA/GGBFS Geopolymer Concrete Beams after Exposure to Elevated Temperatures, Adv Mater Sci Eng, 2017 (2017) 6854043.
[25] W.B. Ren, J.Y. Xu, E.L. Bai, Strength and Ultrasonic Characteristics of Alkali-Activated Fly Ash-Slag Geopolymer Concrete after Exposure to Elevated Temperatures, J Mater Civil Eng, 28 (2016) 04015124.
[26] W.L. Tu, M.Z. Zhang, Behaviour of alkali-activated concrete at elevated temperatures: A critical review, Cement Concrete Comp, 138 (2023) 104961.
[27] M. Guerrieri, J. Sanjayan, F. Collins, Residual compressive behavior of alkali-activated concrete exposed to elevated temperatures, Fire Mater, 33 (2009) 51-62.
[28] S. Sasui, G. Kim, J. Nam, A. van Riessen, M. Hadzima-Nyarko, G. Choe, D. Suh, W. Jinwuth, Effects of waste glass sand on the thermal behavior and strength of fly ash and GGBS based alkali activated mortar exposed to elevated temperature, Constr Build Mater, 316 (2022) 125864.
[29] G.H. Fang, Q. Wang, M.Z. Zhang, In-situ X-ray tomographic imaging of microstructure evolution of fly ash and slag particles in alkali-activated fly ash-slag paste, Compos Part B-Eng, 224 (2021) 109221.
[30] G.H. Fang, Q. Wang, M.Z. Zhang, Micromechanical analysis of interfacial transition zone in alkali-activated fly ash-slag concrete, Cement Concrete Comp, 119 (2021) 103990.
[31] G.H. Fang, M.Z. Zhang, The evolution of interfacial transition zone in alkali-activated fly ash-slag concrete, Cement Concrete Res, 129 (2020) 105963.

[32] I. Ismail, S.A. Bernal, J.L. Provis, R.S. Nicolas, S. Hamdan, J.S.J. van Deventer, Modification of phase evolution in alkali-activated blast furnace slag by the incorporation of fly ash, Cement Concrete Comp, 45 (2014) 125-135.
[33] X. Gao, Q.L. Yu, H.J.H. Brouwers, Apply Si-29, Al-27 MAS NMR and selective dissolution in identifying the reaction degree of alkali activated slag-fly ash composites, Ceram Int, 43 (2017) 12408-12419.
[34] H.L. Ye, A. Radlinska, Fly ash-slag interaction during alkaline activation: Influence of activators on phase assemblage and microstructure formation, Constr Build Mater, 122 (2016) 594-606.
[35] S. Puligilla, P. Mondal, Role of slag in microstructural development and hardening of fly ash-slag geopolymer, Cement Concrete Res, 43 (2013) 70-80.
[36] I. Garcia-Lodeiro, A. Palomo, A. Fernandez-Jimenez, D.E. Macphee, Compatibility studies between N-A-S-H and C-A-S-H gels. Study in the ternary diagram Na_2O-CaO-Al_2O_3-SiO_2-H_2O, Cement Concrete Res, 41 (2011) 923-931.
[37] W.G.V. Saavedra, R.M. de Gutierrez, Performance of geopolymer concrete composed of fly ash after exposure to elevated temperatures, Constr Build Mater, 154 (2017) 229-235.
[38] G.H. Fang, W.K. Ho, W.L. Tu, M.Z. Zhang, Workability and mechanical properties of alkali-activated fly ash-slag concrete cured at ambient temperature, Constr Build Mater, 172 (2018) 476-487.
[39] H. Zhong, M.Z. Zhang, Effect of recycled tyre polymer fibre on engineering properties of sustainable strain hardening geopolymer composites, Cement Concrete Comp, 122 (2021) 104167.
[40] W.L. Tu, Y. Zhu, G.H. Fang, X.G. Wang, M.Z. Zhang, Internal curing of alkali-activated fly ash-slag pastes using superabsorbent polymer, Cement Concrete Res, 116 (2019) 179-190.
[41] Building code requirements for structural concrete (ACI 318-08) and commentary, American Concrete Institute, 2008.
[42] J.T. Xie, O. Kayali, Effect of superplasticiser on workability enhancement of Class F and Class C fly ash-based geopolymers, Constr Build Mater, 122 (2016) 36-42.
[43] M. Chen, Z. Sun, W. Tu, X. Yan, M. Zhang, Behaviour of recycled tyre polymer fibre reinforced concrete at elevated temperatures, Cement and Concrete Composites, (2021) 104257.
[44] H.Q. Ma, C. Wu, Mechanical and microstructural properties of alkali-activated fly ash-slag material under sustained moderate temperature effect, Cement Concrete Comp, 134 (2022) 104744.
[45] G. Fang, H. Bahrami, M. Zhang, Mechanisms of autogenous shrinkage of alkali-activated fly ash-slag pastes cured at ambient temperature within 24 h, Constr Build Mater, 171 (2018) 377-387.
[46] P.S. Singh, T. Bastow, M. Trigg, Structural studies of geopolymers by Si-29 and Al-21 MAS-NMR, J Mater Sci, 40 (2005) 3951-3961.

[47] O. Burciaga-Diaz, J.I. Escalante-Garcia, Structure, Mechanisms of Reaction, and Strength of an Alkali-Activated Blast-Furnace Slag, J Am Ceram Soc, 96 (2013) 3939-3948.
[48] S.A. Bernal, J.L. Provis, B. Walkley, R.S. Nicolas, J.D. Gehman, D.G. Brice, A.R. Kilcullen, P. Duxson, J.S.J. van Deventer, Gel nanostructure in alkali-activated binders based on slag and fly ash, and effects of accelerated carbonation, Cement Concrete Res, 53 (2013) 127-144.
[49] F. Puertas, M. Palacios, H. Manzano, J.S. Dolado, A. Rico, J. Rodriguez, A model for the C-A-S-H gel formed in alkali-activated slag cements, J Eur Ceram Soc, 31 (2011) 2043-2056.
[50] D. Jeon, Y. Jun, Y. Jeong, J.E. Oh, Microstructural and strength improvements through the use of Na2CO3 in a cementless Ca(OH)(2)-activated Class F fly ash system, Cement Concrete Res, 67 (2015) 215-225.
[51] O. Burciaga-Diaz, J.I. Escalante-Garcia, Comparative performance of alkali activated slag/metakaolin cement pastes exposed to high temperatures, Cement Concrete Comp, 84 (2017) 157-166.
[52] L.P. Liu, H.N. Liu, Y. Xu, J.C. Xiang, Y. He, G.J. Zheng, Mechanical Properties and Microstructure of Alkali-Activated Slag Grouting Materials Exposed to Flowing $NaHCO_3$ Solution, J Mater Civil Eng, 34 (2022).
[53] P. Florian, E. Veron, T.F.G. Green, J.R. Yates, D. Massiot, Elucidation of the Al/Si Ordering in Gehlenite Ca2Al2SiO7 by Combined Si-29 and Al-27 NMR Spectroscopy/Quantum Chemical Calculations, Chem Mater, 24 (2012) 4068-4079.
[54] C.L. Chan, M.Z. Zhang, Behaviour of strain hardening geopolymer composites at elevated temperatures, Cement Concrete Comp, 132 (2022) 104634.
[55] H. Schneider, J. Schreuer, B. Hildmann, Structure and properties of mullite - A review, J Eur Ceram Soc, 28 (2008) 329-344.
[56] S.F. Dai, L. Zhao, S.P. Peng, C.L. Chou, X.B. Wang, Y. Zhang, D. Li, Y.Y. Sun, Abundances and distribution of minerals and elements in high-alumina coal fly ash from the Jungar Power Plant, Inner Mongolia, China, Int J Coal Geol, 81 (2010) 320-332.
[57] Z.J. Jia, C. Chen, J.J. Shi, Y.M. Zhang, Z.M. Sun, P.G. Zhang, The microstructural change of C-S-H at elevated temperature in Portland cement/GGBFS blended system, Cement Concrete Res, 123 (2019) 105773.
[58] X. Tian, F. Rao, C.X. Li, W. Ge, N.O. Lara, S.X. Song, L. Xia, Solidification of municipal solid waste incineration fly ash and immobilization of heavy metals using waste glass in alkaline activation system, Chemosphere, 283 (2021) 131240.
[59] G.D. Huang, L. Yuan, Y.S. Ji, B.L. Liu, Z.S. Xu, Cooperative action and compatibility between Portland cement and MSWI bottom ash alkali-activated double gel system materials, Constr Build Mater, 209 (2019) 445-453.

[60] Y. Luo, K.M. Klima, H.J.H. Brouwers, Q.L. Yu, Effects of ladle slag on Class F fly ash geopolymer: Reaction mechanism and high temperature behavior, Cement Concrete Comp, 129 (2022) 104468.
[61] A. Fernandez-Jimenez, A. Palomo, Mid-infrared spectroscopic studies of alkali-activated fly ash structure, Micropor Mesopor Mat, 86 (2005) 207-214.
[62] M.R. Ahmad, L.P. Qian, Y. Fang, A.G. Wang, J.G. Dai, A multiscale study on gel composition of hybrid alkali-activated materials partially utilizing air pollution control residue as an activator, Cement Concrete Comp, 136 (2023) 104856.
[63] M. Lahoti, K.K. Wong, K.H. Tan, E.H. Yang, Effect of alkali cation type on strength endurance of fly ash geopolymers subject to high temperature exposure, Mater Design, 154 (2018) 8-19.
[64] S.Q. Ruan, S.K. Chen, X.Y. Zhu, Q. Zeng, Y. Liu, J.Y. Lai, D.M. Yan, Matrix wettability and mechanical properties of geopolymer cement-polydimethylsiloxane (PDMS) hybrids, Cement Concrete Comp, 124 (2021) 104268.
[65] M. Cyr, R. Pouhet, Carbonation in the pore solution of metakaolin-based geopolymer, Cement Concrete Res, 88 (2016) 227-235.
[66] S. Kumar, R. Kumar, T.C. Alex, A. Bandopadhyay, S.P. Mehrotra, Influence of reactivity of fly ash on geopolymerisation, Adv Appl Ceram, 106 (2007) 120-127.
[67] P.Z. Wang, R. Trettin, V. Rudert, Effect of fineness and particle size distribution of granulated blast-furnace slag on the hydraulic reactivity in cement systems, Adv Cem Res, 17 (2005) 161-166.
[68] Y. Li, K.H. Tan, E.H. Yang, Synergistic effects of hybrid polypropylene and steel fibers on explosive spalling prevention of ultra-high performance concrete at elevated temperature, Cement Concrete Comp, 96 (2019) 174-181.
[69] Y. Li, P. Pimienta, N. Pinoteau, K.H. Tan, Effect of aggregate size and inclusion of polypropylene and steel fibers on explosive spalling and pore pressure in ultra-high-performance concrete (UHPC) at elevated temperature, Cement Concrete Comp, 99 (2019) 62-71.
[70] M. Sivasakthi, R. Jeyalakshmi, N.P. Rajamane, R. Jose, Thermal and structural micro analysis of micro silica blended fly ash based geopolymer composites, J Non-Cryst Solids, 499 (2018) 117-130.
[71] M.R. Ahmad, M. Khan, A.G. Wang, Z.H. Zhang, J.G. Dai, Alkali-activated materials partially activated using flue gas residues: An insight into reaction products, Constr Build Mater, 371 (2023) 130760.
[72] K. Traven, M. Cesnovar, S.D. Skapin, V. Ducman, High temperature resistant fly-ash and metakaolin-based alkali-activated foams, Ceram Int, 47 (2021) 25105-25120.

[73] R.L. Burwell, Manual of Symbols and Terminology for Physicochemical Quantities and Units - Appendix 2 - Definitions, Terminology and Symbols in Colloid and Surface-Chemistry .2. Heterogeneous Catalysis, Pure Appl Chem, 46 (1976) 71.
[74] L.M. Anovitz, D.R. Cole, Characterization and Analysis of Porosity and Pore Structures, Rev Mineral Geochem, 80 (2015) 61.
[75] S. Diamond, Mercury porosimetry - An inappropriate method for the measurement of pore size distributions in cement-based materials, Cement Concrete Res, 30 (2000) 1517-1525.
[76] H.Y. Ma, Mercury intrusion porosimetry in concrete technology: tips in measurement, pore structure parameter acquisition and application, J Porous Mat, 21 (2014) 207-215.
[77] Y. Peng, G.R. Zhao, Y.X. Qi, Q. Zeng, In-situ assessment of the water-penetration resistance of polymer modified cement mortars by mu-XCT, SEM and EDS, Cement Concrete Comp, 114 (2020) 103821.
[78] S.Q. Ruan, D.M. Yan, S.K. Chen, F.X. Jiang, W.W. Shi, Process and mechanisms of multi-stage water sorptivity in hydrophobic geopolymers incorporating polydimethylsiloxane, Cement Concrete Comp, 128 (2022) 104460.
[79] C.J. Shi, A.F. Jimenez, A. Palomo, New cements for the 21st century: The pursuit of an alternative to Portland cement, Cement Concrete Res, 41 (2011) 750-763.